Science of the Total Environment 764 (2021) 144255

Contents lists available at ScienceDirect

Science of the Total Environment

journal homepage: www.elsevier.com/locate/scitotenv

Modeling linkages between erosion and connectivity in an urbanizing landscape

Alexander Michalek, Amirreza Zarnaghsh, Admin Husic *

Dept. of Civil, Environmental and Architectural Engineering, University of Kansas, United States of America

HIGHLIGHTS

- Erosion limits sediment transport more often than connectivity.
- Urbanization augments connectivity and increases sediment conveyance.
- Erosion-connectivity mapping bridges *RUSLE* and *IC* methodologies.
- Fieldwork shows that geospatial models underpredict erosion-connectivity coupling.

GRAPHICAL ABSTRACT

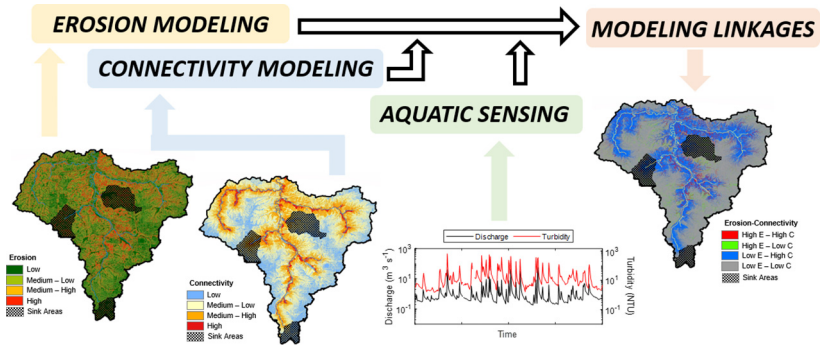

ARTICLE INFO

Article history:
Received 12 August 2020
Received in revised form 25 November 2020
Accepted 26 November 2020
Available online xxxx

Editor: Paulo Pereira

Keywords:
Disconnectivity
RUSLE
Index of Connectivity
Sediment Delivery Ratio

ABSTRACT

Erosion and connectivity are spatially varied processes key to determining sediment transport and delivery to downstream waterbodies. However, we find few studies that explicitly model the linkages of where erosion and connectivity coincide and where they contradict, particularly in urbanizing settings. In this study, we couple in-stream aquatic sensing, the Revised Universal Soil Loss Equation (RUSLE), the Index of Connectivity (IC), and the Sediment Delivery Ratio (SDR), together with Monte Carlo uncertainty analysis, to generate a new Erosion-Connectivity Mapping (ECM) framework. We evaluate ECM accuracy with field assessment of thirty-five sites spread across five lowland watersheds (mean slope <5°) in Johnson County, Kansas, USA, which differ primarily in their land use, ranging from 21% to 89% urban. RUSLE modeling results indicate erosion is controlled by topography with high risk areas near streambanks roadway systems. SDR and IC were positively related at the five sites ($R2 = 0.78$, $p < 0.05$) with the highest values in the most urbanized watershed, indicating that anthropogenic change augments connectivity. The ECM results indicate that while only 5±1% of the study area is both highly erodible and highly connected, these areas represent 37±4% of total watershed-scale erosion. Our modeling results indicate that erosion is more likely to be the limiting factor in sediment transport, as opposed to connectivity, as there are generally more locations that are well-connected to hydrologic transport but resistant to erosion. Our field assessment provided broad support for the ECMs; however, field assessment indicated that geospatial modeling underpredicts how closely related erosion and connectivity are in the field and we suggest that future models consider this coupling more explicitly. This study provides a method for combining RUSLE and IC in a new tool (ECM) to identify spatial patterns in sediment erosion-connectivity to aid in the understanding and management of watershed sedimentation.

* Corresponding author at: 2134B Learned Hall, University of Kansas, Lawrence, KS 66045, United States of America.
E-mail address: ahusic@ku.edu (A. Husic).

https://doi.org/10.1016/j.scitotenv.2020.144255
0048-9697/

1. Introduction

Anthropogenic activity exacerbates sediment erosion from the uplands and connectivity to downstream receiving bodies, which in turn has negative impacts to agricultural profitability, geomorphic stability, and in-stream aquatic health (Heathcote et al., 2013; van der Waal and Rowntree, 2018; Llena et al., 2019). This problem is likely to continue as global modeling projections indicate a doubling of the world's urban population by the end of the 21st century, which will be accompanied by landscape urbanization to satisfy population demands (Jiang and O'Neill, 2017). Urbanizing landscapes increase the potential for erosion through the removal of soil surface preserving factors, such as vegetative buffers, which expose sediment sources to transport. Further, urbanized landscapes contain greater densities of impervious areas, generate higher magnitude runoff, and increase transport capacity of runoff (Hu et al., 2001), thus augmenting the connectivity of sediment from source to sink. In the past few years, many researchers have investigated erosion and connectivity (Hui et al., 2010; Soohoo et al., 2017; Bordoni et al., 2018; Mahoney et al., 2018), but we find a lack of study aimed at modeling their linkages, an understanding of which could provide improved land management strategies for minimizing soil loss under anthropogenic land use change.

As erosion is difficult to measure at the watershed-scale, geospatial modeling coupled to in-stream monitoring provides a cost-effective method for modeling integrated sediment erosion (Beskow et al., 2009; Yuan et al., 2016; Grauso et al., 2018). The Revised Universal Soil Loss Equation (*RUSLE*) has emerged as the most common method for estimating geospatial soil erosion and has been applied to mountainous and lowland areas (Ozcan et al., 2008; Soohoo et al., 2017; Ozsahin et al., 2018; Zhao et al., 2020), ranging in watershed areas from < 1 km^2 to millions of km^2 (Borrelli et al., 2012; Napoli et al., 2016; Zeng et al., 2017; Zerihun et al., 2018). *RUSLE* takes into consideration geospatial data relating to topography, land cover, pedology, land management, and rainfall intensity to predict annual-scale sediment erosion (Smith and Wischmeier, 1962; Renard et al., 1997; Hamel et al., 2017; Singh and Panda, 2017). Since some factors, such as the erodibility of a particular land use, may be difficult to parameterize, statistical methods such as Monte Carlo sampling can be used to assess parameter uncertainty (Papadopoulos and Yeung, 2001; Harrison, 2009; Martin and Ayesa, 2010). Other limitations of *RUSLE* are that it is not applicable to single storm event analysis (unlike *MUSLE*), does not account for gully or channel erosion, and does not explicitly represent hydrologic and erosion processes as it is an empirical model (Renard et al., 2008). In situ sensing of stream discharge and sediment concentration (or turbidity) allows for the calculation of sediment yields and the investigation of a watershed's efficiency for exporting eroded material, termed the Sediment Delivery Ratio (*SDR*) (Borselli et al., 2008; Beskow et al., 2009; Hui et al., 2010; Hamel et al., 2017; Grauso et al., 2018; Heckmann and Vericat, 2018; Zhao et al., 2020). Despite the widespread development and deployment of these tools, we find few cases in the literature (López-vicente et al., 2013; Zhao et al., 2020) that investigate sediment erosion and delivery across actively urbanizing landscapes.

Sediment connectivity is defined as the degree to which a system facilitates the transfer of water and sediment through the spatial arrangement of geomorphic features and processes (Heckmann et al., 2018). Two types of connectivity emerge from this definition: structural and functional. Structural connectivity is the spatial configuration of system components whereas functional connectivity represents the dynamic spatiotemporal processes of a system (Heckmann et al., 2018). Structural connectivity indices are more commonly applied (Cavalli et al., 2013; López-vicente et al. 2013; Tiranti et al., 2018; Tarolli et al., 2019) as they require only topographic data. The Index of Connectivity (*IC*), developed by Borselli et al. (2008), is a commonly used method for numerically modeling sediment connectivity at the catchment scale and has been applied to examine the effect of land use change, rilled hillslope connectivity, and landslide susceptibility (Cavalli et al., 2013; Tiranti et al., 2018; Llena et al., 2019; Lu et al., 2019). Though it was developed for mountainous regions, the *IC* has also been applied successfully to lowland settings although care must be taken as *IC* may overpredict hotspots of connectivity in lowlands as it does not consider factors other than topography that can control disconnectivity in an area (e.g. buffers) (Fryirs, 2012; Gay et al., 2016; Calsamiglia et al., 2018; Husic et al., 2020). The simplicity of the index makes it an attractive tool for assessing connectivity as it requires very little data and is not computationally intense, allowing for large-scale and/or fine-resolution application (Cavalli et al., 2013; Crema and Cavalli, 2018; Husic et al., 2020; Mahoney et al., 2018; Tarolli et al., 2019). However, the *IC* does not entirely account for soil surface characteristics that affect runoff in lowland areas and as such it should be accompanied by either index revision or complimentary field campaigns (Gay et al., 2016). A field assessment allows for connectivity observations to be fitted to the study area to examine unaccounted for connectivity process that are highly complex, especially in urbanizing settings.

The capability of a land parcel to be eroded does not necessarily entail its connection to downstream waterbodies due to blockages in the sediment cascade, a process known as (dis)connectivity (Fryirs, 2012). (Dis)connectivity occurs because the geomorphic processes responsible for sediment erosion (e.g., channel geometry and weathering) can differ from those responsible for connectivity (e.g., sediment cascade blockages) (Cavalli et al., 2013; Hamel et al., 2017; Heckmann et al., 2018). Relatively little is known regarding the spatial variability in erosion-connectivity linkages, or where these processes coincide (i.e. couplings) and where they contradict (i.e. (de)couplings). Until very recently, most geospatial modeling work has applied either erosion (Ozcan et al., 2008; Biswas and Pani, 2015; Rizeei et al., 2016; Lisboa et al., 2017) or connectivity (Cavalli et al., 2013; Bordoni et al., 2018; Calsamiglia et al., 2018; Tiranti et al., 2018; Tarolli et al., 2019) independently to examine sediment transport. Some new tools explicitly simulate connectivity and erosion but require extensively-calibrated hydrologic and sediment transport models (Mahoney et al., 2018, 2020a, 2020b) that are more data-intensive than geospatial index models. Only a few studies (Hamel et al., 2017; Zhao et al., 2020), to our knowledge, have applied *RUSLE* and *IC* in a single analysis with Zhao et al. (2020) relating the calculations to examine sediment load variations attributable to land use change over time. However, new geospatial modeling tools for elucidating where erosion and connectivity linkages are coupled and (de) coupled are needed for more informed land management. Further, such models should be extensively validated by field reconnaissance to assess accuracy of process representation and limits of model applicability.

Overall, this study aims to understand how sediment erosion and connectivity are linked across an urbanizing lowland landscape with the following objectives: (1) apply the *RUSLE* and *IC* models to five watersheds across an urbanization gradient, (2) identify anthropogenic influences on spatial gradient of erosion and connectivity, and (3) identify couplings and (de)couplings of sediment erosion and connectivity using new modeling and field assessment approaches.

2. Study site and materials

2.1. Study site

Johnson County (1235 km^2) is a rapidly urbanizing area in northeastern Kansas (Fig. 1a) that has seen a population increase of about 32% from 2000 to 2018, making it the most rapidly developing area in Kansas (Rasmussen and Gatotho, 2014). The county constitutes the southwestern quadrant of the Kansas City metropolitan area, which has a population of over 2 million people. The land cover shift from urban to agricultural is distinct and indicates an urban sprawl from Kansas City (northeast) into rural Johnson County (southwest) (Fig. 1b). The broader geographical region is characterized as lowland plains with an average slope of 3.7° and a temperate climate (MAT: 13.1 °C; MAP:

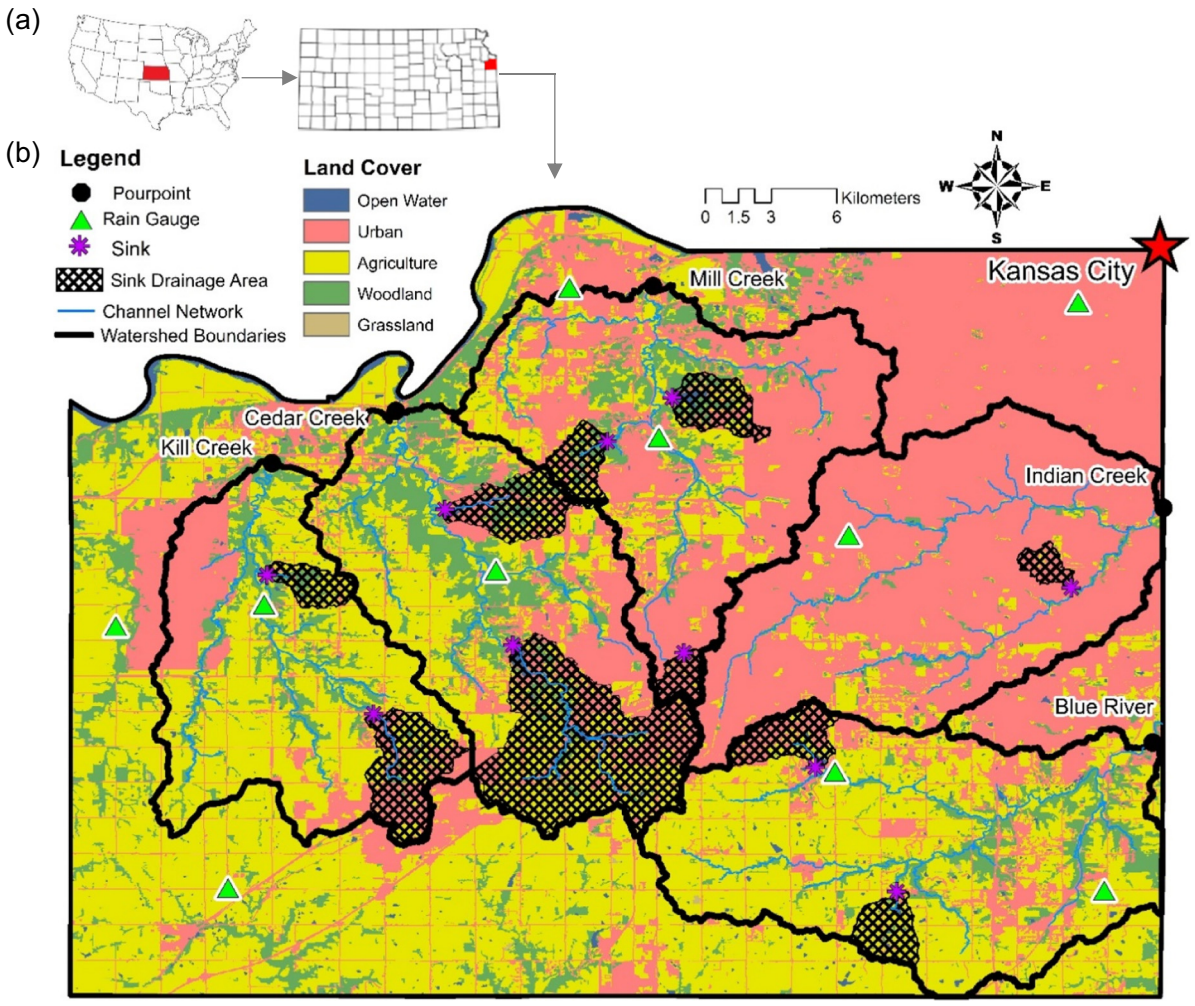

Fig. 1. (a) Location of Johnson County, Kansas in reference to location in the United States. (b) Pour point locations, rain gages, stream networks, sinks (e.g. lakes and reservoirs), and land use for Kill Creek, Cedar Creek, Mill Creek, Indian Creek, and Blue River. (For interpretation of the references to colour in this figure legend, the reader is referred to the web version of this article.)

958 mm). In this work, we focused on the five largest watersheds in Johnson County: Blue River (170 km^2), Kill Creek (130 km^2), Cedar Creek (123 km^2), Mill Creek (150 km^2), and Indian Creek (168 km^2) (Table 1). The watersheds are similar in their drainage areas, rainfall, and average slopes, but they differ vastly in land use. Indian Creek (89.4%) and Mill Creek (61.8%) are mostly urbanized while Cedar Creek (30.5%), Kill Creek (26.4%), and Blue River (21.1%) are less urbanized. There were major sinks, such as reservoirs, lakes, dams, and quarries that removed flow from transport, and we have delineated the sink drainage area for each of these. As land-cover is the major feature that substantially differs across the watersheds, the study sites provide an opportunity for us to examine how the degree of urbanization impacts erosion and connectivity across urban, mixed, and agricultural landscapes.

2.2. Materials

High-resolution turbidity and discharge data, collected and maintained by the United States Geological Survey (USGS, 2018), were used to calculate sediment yield for this study (2004 to 2007). USGS stations are located at the downstream parts of the watersheds (Fig. 1b). Turbidity data were collected by high-frequency sensors installed at the monitoring stations while discharge was predicted by stage-discharge rating curves for each station. Thirty-minute rainfall data from ten stations in Johnson County were download from the period of 2002 to 2008 (StormWatch, 2020) (Fig. 1b). Land surface datasets for landcover and soil composition (Fig. S1) were downloaded from National Land Class Database (NLCD, 2015) and the National Cooperative

Table 1
Drainage area, average slope, annual rainfall, and land use characteristics of the studied watersheds. Watersheds are ordered from least to most urban.

Watershed	Area (km^2)	Average Slope (°)	Average Rainfall (mm/yr)	Urban	Agriculture	Forest	Grassland	Water
Blue River	170	3.5	955	21.1%	64.1%	13.0%	0.6%	1.2%
Kill Creek	130	3.5	968	26.4%	55.4%	16.4%	0.8%	1.0%
Cedar Creek	153	4.3	935	30.5%	43.9%	22.3%	2.0%	1.3%
Mill Creek	150	3.5	960	61.8%	23.4%	13.6%	0.6%	0.6%
Indian Creek	168	3.5	973	89.4%	6.8%	3.2%	0.4%	0.2%

Soil Survey over the course of a century (USDA, 2018), respectively. The land cover data was provided at 30-m resolution with a 16-class legend based on an Anderson Level II classification system with a range of agreement from 71% to 97% depending upon site location (NLCD, 2015). The RUSLE model in this study deployed high-resolution 1-m digital elevation maps (DEMs) provided by Johnson County Automated Information Mapping System (AIMS, 2020).

3. Methods

We developed the following workflow to address our research objectives (Fig. 2):

a) Erosion Modeling: to convert raster data sets into spatial sediment erosion maps and perform uncertainty analysis on land cover factors;
b) Aquatic Sensing: to integrate stream discharge and sediment turbidity data to determine sediment yield at watershed pourpoints;
c) Connectivity Modeling: to map sediment connectivity using *IC*, convert sediment yield to *SDR*, and examine the relationship between study sites;
d) Linkage Analysis: to obtain a singular map linking erosion and connectivity modeling and validate with field assessment.

3.1. Sediment erosion modeling

3.1.1. Revised Universal Soil Loss Equation

Our study used the Revised Universal Soil Loss Equation (*RUSLE*) to spatially model soil loss at a 1 m × 1 m grid resolution to classify erosion prone areas (Renard et al., 1997). The *RUSLE* model is a function of climate, soil, topography, and land use. The annual soil loss per grid cell is calculated based on the following equation:

$$A = RKLSCP \quad (1)$$

where A is the soil loss per area (tons ha^{-1} yr^{-1}), R is the rainfall erosivity or rainfall and runoff factor in a select area (MJ mm ha^{-1} h^{-1} yr^{-1}), K is the soil erodibility factor for each soil type (ton ha h ha^{-1} MJ^{-1} mm^{-1}), L is the slope length factor (unitless) and is the ratio of soil loss from a field's slope length to the soil loss from a reference plot size of 72.6′, S is the slope steepness factor (unitless) and is the ratio of soil loss from the field slope to the soil loss from a reference slope of 9% slope, C is the cropping management factor (unitless) that is the ratio of soil loss for a specified land cover to the soil loss, and P is the erosion control practice factor (unitless) (Wischmeier and Smith, 1978).

Rainfall erosivity was estimated by classifying storm events as the total rain amount per day using 30-min rainfall data at 10 rainfall stations across Johnson County (Fig. 1b). Inverse distance weighting was used to develop the erosivity gradient across all five watersheds (Ozsahin et al., 2018; Zhao et al., 2020). The soil erodibility factor (K) at a 10-m resolution was publicly available to download from the United States Department of Agriculture (USDA, 2018) using their Soil Data Viewer extension for ArcGIS (ESRI, 2006). Erodibility in the Soil Data Viewer tool is a function of percentage of silt, sand, and organic matter as well as soil structure and saturated hydraulic conductivity. The *LS* factor was estimated using the Moore and Burch equation based on flow accumulation (Ozsahin et al., 2018) as the geomorphology was spatially consistent. The cropping management factor (C) was determined based on literature-reported values of land cover type (Table S1 and references therein). From our literature review of thirty-two studies, we found that reported C factors varied considerably, even for the same land use description. Thus, in our *RUSLE* modeling, we performed Monte Carlo sampling to assess how C factor uncertainty propagates into erosion modeling estimates. Due to the lack of information regarding erosion practices in Johnson County the erosion control practice factor (P) was taken as 1.0 (Renard et al., 1997).

3.1.2. Monte Carlo uncertainty analysis

In this study, Monte Carlo simulation was used to assess how subjective selection of cropping management factors (C) affects uncertainty in *RUSLE* erosion prediction. We aggregated thirty-two studies from the *RUSLE* literature and generated discrete statistical distributions of C factors for each land class (Table S1). The C values ranged from 0 to 1, 0–0.32, 0–0.32, and 0–0.8 for agricultural, forest, grassland, and urban classes, respectively. Two hundred simulations were performed for each year of the study period (2001–2007). For each simulation, individual C factors were randomly sampled from their respective parent statistical distributions. Thereafter, the *RUSLE* model was executed and average erosion for each watershed was estimated using the Mean Zonal Statistics function in ArcGIS. Lastly, we report mean and standard

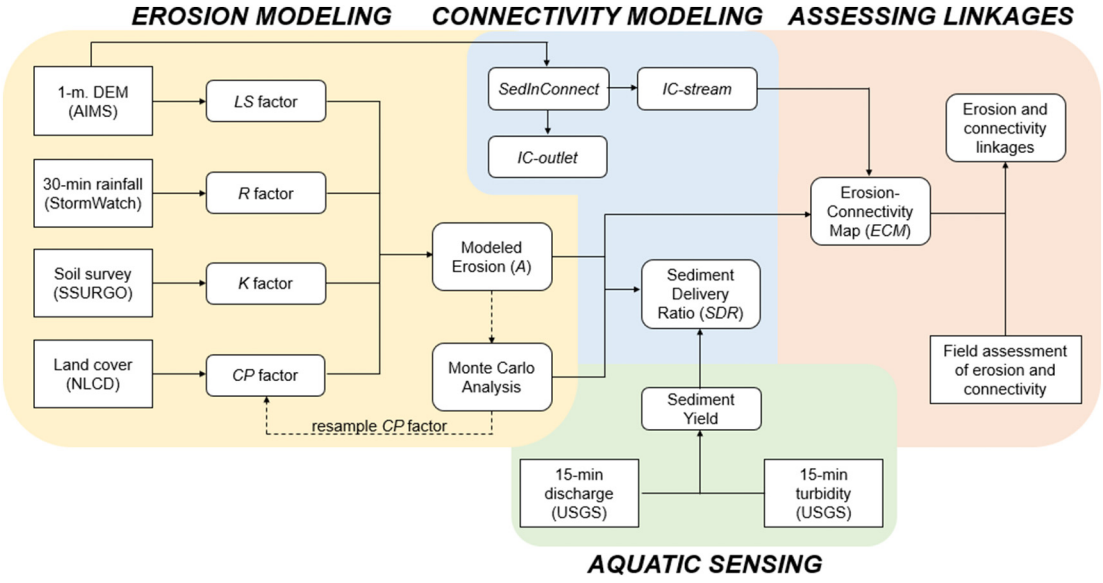

Fig. 2. The workflow of erosion and connectivity modeling and analysis of erosion-connectivity linkages. Sharp cornered boxes indicate datasets with the data-source listed in parenthesis. Round boxes represent modeled products. Dashed-lines indicate Monte Carlo simulations and re-sampling of the *CP* factor to generate erosion uncertainty bounds.

deviation values using the 95% prediction interval of all Monte Carlo simulations.

3.2. Sediment connectivity analysis

3.2.1. Sediment Delivery Ratio

The sediment delivery ratio (*SDR*) is defined as the ratio between sediment yield at a watershed pourpoint and the average annual soil loss across the upstream watershed (Zhao et al., 2020). The *SDR* is a common indicator (Brierley et al., 2006; Rommens et al., 2006; Baartman et al., 2013; Di Stefano and Ferro, 2019) used as a proxy for catchment connectivity at the most basic level with values approaching 1 indicating full connectivity (Gay et al., 2016). *SDR* is interpreted as a reflection of sediment connectivity between water networks and land surface sediment sources and is used as a black box measure of watershed scale (dis)connectivity (Najafi et al., 2021). In this study, the *SDR* was modeled using the *RUSLE* model and sediment yield estimated by the following equation:

$$S_y = \frac{SDR \cdot \left(\sum_i^n E_i\right)}{A_w} \tag{2}$$

where S_y is the sediment yield (tons ha^{-1} yr^{-1}), $\sum_i^n E_i$ is the total erosion from each source in the watershed (tons yr^{-1}), and A_w is the watershed area (acres). Sediment yield was estimated using aquatic sensing data as follows:

$$S_y = \int Q_{ss} \cdot dt \tag{3}$$

where:

$$Q_{ss} = Q \cdot C_s \tag{4}$$

where Q is the discharge at an hourly time interval (m^3 s^{-1}), C_s is the suspended sediment concentration (mg L^{-1}) determined from transforming turbidity measurements (NTU) at hourly resolution from USGS using regression equations (Table S2), and *Qss* is the sediment load (ton hr^{-1}) at each time step. The sediment yield integral was discretized and approximated numerically.

3.2.2. Index of Connectivity

The Index of Connectivity (*IC*) developed by Borselli et al. (2008) was used to represent structural sediment connectivity and is described as the probability of sediment from an upslope point to travel downslope to a local sink or target. *IC* is empirically defined by Borselli et al. (2008) as:

$$IC = \log_{10}\left(\frac{D_{up}}{D_{dn}}\right) \tag{5}$$

where D_{up} and D_{dn} identify the upslope and downslope elements of connectivity, respectively. The *IC* can range from $[-\infty, +\infty]$ with greater values indicating higher connectivity.

The upslope component D_{up} describes the potential of sediment yields from upslope sources to be routed downward and is approximated as:

$$D_{up} = \overline{W} \cdot \overline{S} \cdot \sqrt{A} \tag{6}$$

where $\overline{W}$ is the average weighting factor of the contributing upslope area, $\overline{S}$ is the average slope of the contributing upslope area (m/m) and A is the contributing upslope area (m^2).

The downslope component D_{dn} describes the probability of the sediment flow to travel along the flow path arriving at the nearest target or sink and is estimated as:

$$D_{dn} = \sum_i \frac{d_i}{W_i \cdot S_i} \tag{7}$$

where d_i is the length of the flow path to the downstream channel along the i^{th} cell at the steepest slope direction (m). W_i is the weighting factor at the i^{th} cell and S_i is the slope gradient at the i^{th} cell.

The weighting factor *W* was originally introduced in Borselli et al. (2008) to account for surface characteristics that affect runoff and sediment flux processes. Borselli et al. (2008) estimated this parameter by using the *C*-factor from *RUSLE* but later findings by Cavalli et al. (2013) showed the use of the surface roughness or roughness index (*RI*) better simulates surface characteristics. The *RI* is the standard deviation of the residual topography computed over a 5×5 cell moving window (Cavalli et al., 2013) and is calculated as:

$$RI = \sqrt{\frac{\sum_{i=1}^{25} (x_i - x_m)^2}{25}} \tag{8}$$

where x_i is the value of the i^{th} cell of the residual topography within the moving window and x_m is the mean of the cells in the 5×5 cell window. The weighting factor *W* is then defined as:

$$W = 1 - \left(\frac{RI}{RI_{MAX}}\right) \tag{9}$$

with R_{MAX} as the maximum value of *RI* across the study sites.

The *IC* in this study was modeled using the *SedInConnect* standalone tool developed by Crema and Cavalli (2018). *SedInConnect* has the main components consisting of Surface Roughness, Weighting Factor, Connectivity Index Targets, and sink targets. The original DEM raster is used to find the surface roughness based on a set moving window to calculate the weighting factor. The Connectivity Index subset allows for the *IC* to be calculated at either a specified target or the pourpoint. Sink features can be added to mask areas from *IC* analysis in the calculation of the distribution of value. In this work, the IC was calculated for major streamways for each watershed with values being normalized based on watershed for spatial comparison. Additionally, the *IC* using the pourpoint as target was calculated for each watershed to validate the use of stream targets for spatial analysis. To maintain consistency across watersheds when computing the stream-target *IC*, Soil and Water Assessment Tool (*SWAT*) was used to identify main runoff targets. *SWAT* uses ArcHydro feature to determine the stream definition using a threshold of 1% of maximum flow accumulation (ESRI ArcMap 10.3). All watersheds converge to fourth order networks. Finally, major sink areas (Fig. 1b) were added for large reservoirs, lakes, and quarries to understand how masking these areas (i.e. excluding them from downstream connectivity) would affect analysis.

3.3. Sediment erosion and connectivity linkages

3.3.1. Erosion-Connectivity Mapping

We developed the Erosion-Connectivity Mapping (ECM) framework to geospatially model the couplings and (de)couplings of erosion and connectivity. First, erosion and stream target *IC* estimates were normalized between 0 and 1, respectively, and kernel density functions of the estimates were made for each watershed. Thereafter, Erosion-Connectivity Biplots (ECBs) were generated by plotting the *IC* kernel on the x-axis and the erosion kernel on the y-axis. Each *ECB* was segregated into four quadrants: high erosion & high connectivity (*E-C*), high erosion & low connectivity (*E-c*), low erosion & high connectivity (*e-C*), and low erosion & low connectivity (*e-c*). Quadrant break points were determined using the Jenks natural breaks algorithm (Jenks, 1967). Jenks natural breaks set the most effective class limits for similar values while maximizing the difference between classes as used in similar applications by Bordoni et al. (2018) and Tiranti et al. (2018). ECMs were then generated by assigning each 1 m × 1 m grid cell in the study area an

ECB quadrant designation (*E-C, E-c, e-C,* or *e-c*). To assess uncertainty within the ECM framework, Monte Carlo simulations from the erosion analysis were used to generate ECB and ECM solution sets. A subset of 25 (of the 200 total) Monte Carlo sets were used because generating hundreds of maps, for each watershed, was computationally intensive. The subset of 25C-factor maps were selected to represent the overall data distribution of the 200 total simulations. Additionally, each run was computed across the 7-year period resulting in a total of 175 data points. Statistics, such as the percent watershed area falling within each ECB quadrant, were calculated as the mean and standard deviation of all Monte Carlo simulations.

3.3.2. Field assessment of erosion-connectivity

Field assessment was performed to verify ECM model results and investigate limitations. Thirty-five field locations (7 in each of the 5 watersheds) were chosen to get equal coverage of all four modeled ECM quadrants (*E-C, E-c, e-C,* and *e-c*). In the field, we surveyed 10 subfactors for erosion and 10 subfactors for connectivity (Table S3). Each subfactor score ranged from 0 to 15, resulting in a maximum score of 150, which would indicate high erosion or connectivity, and a minimum score of 0, which would indicate low erosion or connectivity. To avoid bias due to sediment flows or large runoffs from storm events, site observations were made in similar weather conditions with minimal rainfall before each visit. The ECM was evaluated, and its limits investigated, by comparing how well-correlated erosion and connectivity were predicted by the ECM versus how well-correlated they were observed in the field. This relation was done using linear regression and statistical significance testing ($\alpha = 0.05$).

Subfactors for assessment were compiled from erosion and connectivity literature. Field connectivity subfactors were natural buffer presence (Marchamalo et al., 2016), distance to local sink (Borselli et al., 2008), land cover variability (Mahoney, 2020), presence of visible pathways (Tiranti et al., 2018), subsurface flow paths (Calsamiglia et al., 2018), amount of exposed bare soil (Borselli et al., 2008), presence of deposition (Borselli et al., 2008), amount of visible disconnected plains (Mishra et al., 2019), presence of erosion control features (Marchamalo et al., 2016), and presence of incised channels (Tiranti et al., 2018). Factors such as land cover, subsurface flow paths, deposition, soil sources, and erosion control features are not directly incorporated into the *IC* concept making it important to capture due to anthropogenic influence in the area. Field erosion subfactors were composed of presence of deposition (Borselli et al., 2008), depth of vegetation roots (Mahoney, 2020), amount of sediment sources (Cavalli et al., 2013), presence of uncompacted soil (Borselli et al., 2008), composition of sink (Calsamiglia et al., 2018), presence of depression stores (Messenzehl et al., 2014), channel slope (Cavalli et al., 2013), amount of canopy cover (Mahoney, 2020), and lateral coverage of erosion relative to sink (Mishra et al., 2019). Examination of sediment sources, vegetation cover, and overall spatial extent of process are important to examine due to the lack of resolution for land cover in *RUSLE* with natural presence in urban areas not represented in the *C*-factor.

4. Results and discussion

4.1. Sediment erosion modeling

RUSLE factors for sediment erosion prediction varied considerably along the urbanization gradient in Johnson County, KS (Fig. 3). The rainfall erosivity factor (*R*) varied within the range of 3727 to 5736 MJ-mm-[ha-h-yr]$^{-1}$ across the watersheds (Fig. 3a), indicating a climatically

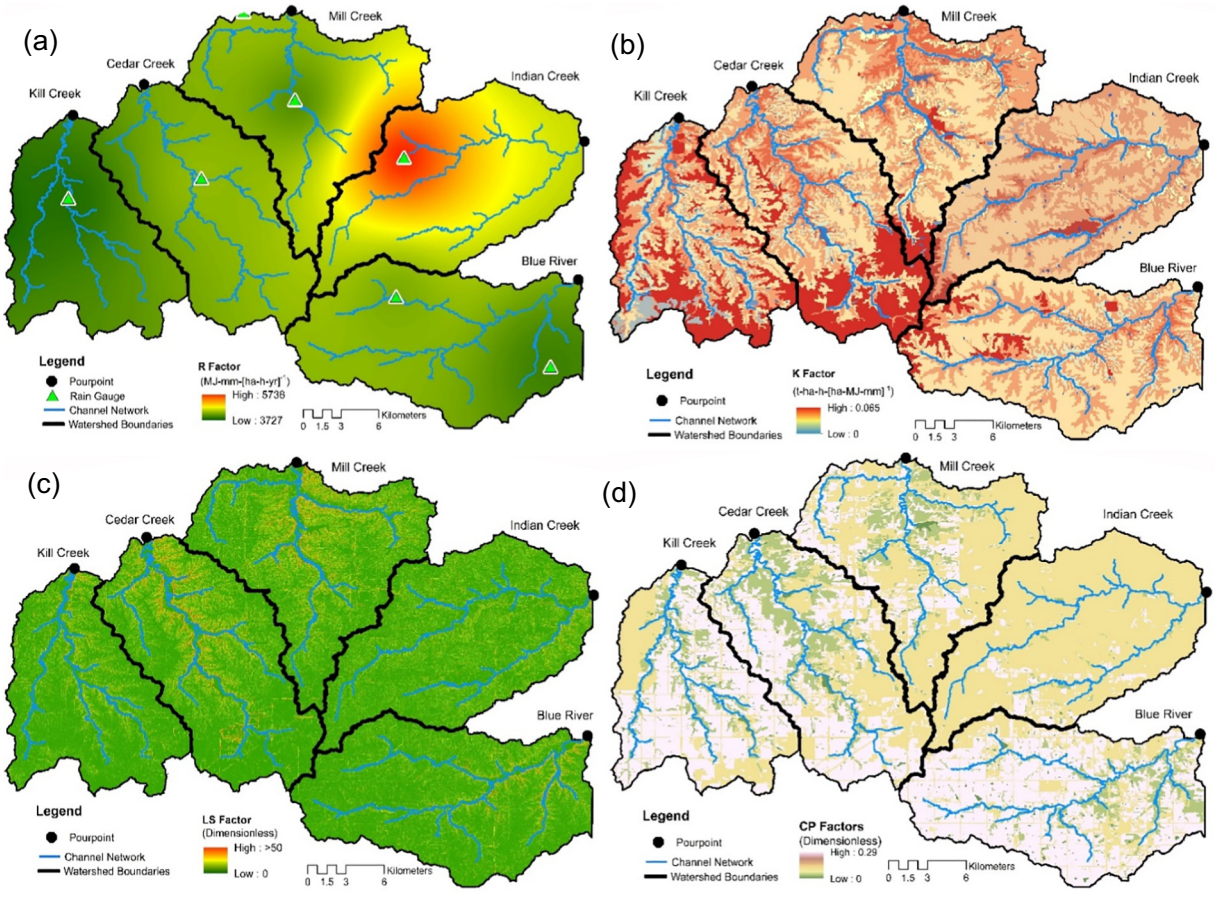

Fig. 3. Spatial distribution maps of (a) rainfall erosivity (*R*-factor), (b) soil erodibility (*K*-factor), (c) slope length and steepness (*LS*-factor), and (d) crop management (*CP*-factor).

high potential for generating erosion. The average rainfall erosivity was 3966, 4272, 4442, 4851, and 4221 for Kill Creek, Cedar Creek, Mill Creek, Indian Creek, and Blue River, respectively. The highest *R* factor values corresponded to Indian Creek, the most urban watershed, whereas a more homogeneous pattern can be observed across the four other watersheds. The soil erodibility factor (*K*) values were within the range of 0 to 0.065 ton-hectare-h- [ha-MJ-mm]$^{-1}$ for the study watersheds (Fig. 3b). Easily erodible soils can be observed in relatively larger areas in the Kill Creek and Cedar Creek watersheds, which can be explained by the larger percentage of loosely bound sandy soils in their texture. Whereas, the Mill Creek, Indian Creek, and Blue River watersheds were mostly occupied by less erosion-sensitive soils with less sand in their soil composition. Spatially, watershed-average *LS* factor values were higher in Cedar Creek (1.26) and Mill Creek (1.34) as opposed to Kill Creek (0.82), Blue River (0.87), and Indian Creek (0.88), indicating that these two watersheds have slope lengths and gradients more prone to erosion (Fig. 3c). In particular, the near-channel areas for the Cedar and Mill watersheds show considerable variability in the magnitude of the *LS* factor, whereas this same degree of variability was not observed for the other watersheds. Fig. 3d shows the *C* factor map for the five land-uses identified in this study: open water, forest, grassland, urban, and agriculture. The average *C* factor values for the land uses were 0, 0.04, 0.08, 0.1, and 0.29, respectively. Blue River (0.21) and Kill Creek (0.20), the most agriculturally dominated watersheds, were generally characterized by larger *C* values, indicating landscape susceptibility to erosion, likely due to cropland. Indian Creek had relatively lower average *C* values (0.11) as it is mostly covered with urban features. Mill Creek (0.14) and Cedar Creek (0.17) contain several dominant land covers, including developed lands, deciduous trees, and cultivated crops and thus have larger variability in *C* factor compared to the other watersheds.

RUSLE modeling results showed large spatiotemporal variability in average annual erosion with high losses concentrated around streambanks and low losses in distal ridges (Fig. 4). The large spatiotemporal variability in modeled annual erosion was primarily a result of variations in the *R*, *LS*, and *C* factors. The average annual erosion of all watersheds was 20.2±13.0 tons ha^{-1} (Table 2). The watersheds ranked in order from greatest to least mean annual erosion were Mill Creek, Cedar Creek, Blue River, Kill Creek, and Indian Creek. Mill Creek (27.1 tons ha^{-1}) and Cedar Creek (25.6 tons ha^{-1}) had the highest erosion estimates due to the combination of steeper slopes near channel networks, considerable areas of erosion-prone agricultural land, and a high concentration of erodible soils. Indian Creek (17.2 tons ha^{-1}) and Kill Creek (17.5 tons ha^{-1}) had relatively lower erosion rates which can be explained by smaller *LS* factors compared to the other watersheds. Smaller *C* values corresponding to the urban landscapes in Indian Creek and lower *R* factors during the study period in Kill Creek are other factors contributing to reduced soil erosion estimates in these two watersheds. Intermediate amounts of erosion occurred in Blue River (22.7 tons ha^{-1}) because its large *C* factor was balanced by poorly erodible soils and short slope lengths/gradients. However, we recognize that *RUSLE* only simulates rill and inter-rill erosion, so these results are only a fraction of the total sediment yield and channelized erosion likely contributes variably in a manner not described by *RUSLE*.

In our review of *C* factors for landscape erosion susceptibility, we found few studies (Alk et al., 2009; Lisboa et al., 2017; Soohoo et al.,

Table 2
Watershed erosion and sediment delivery ratio (*SDR*) results. Measured yield (2004 to 2007) was determined from turbidity sensor data. Modeled erosion (2001 to 2007) was estimated using *RUSLE*. Results are presented as the mean (±1σ) from two-hundred Monte Carlo realizations. Watersheds are ordered from least to most urban.

Watershed	Measured Yield (tons/yr)	Modeled Erosion (tons/ha)	Mean *SDR*
Blue River	28,751 ± 15,227	22.7 ± 11.9	0.07
Kill Creek	7496 ± 4219	17.5 ± 9.6	0.03
Cedar Creek	20,711 ± 11,260	25.6 ± 13.4	0.05
Mill Creek	27,887 ± 13,311	27.1 ± 17.1	0.07
Indian Creek	43,141 ± 12,815	17.2 ± 14.8	0.15

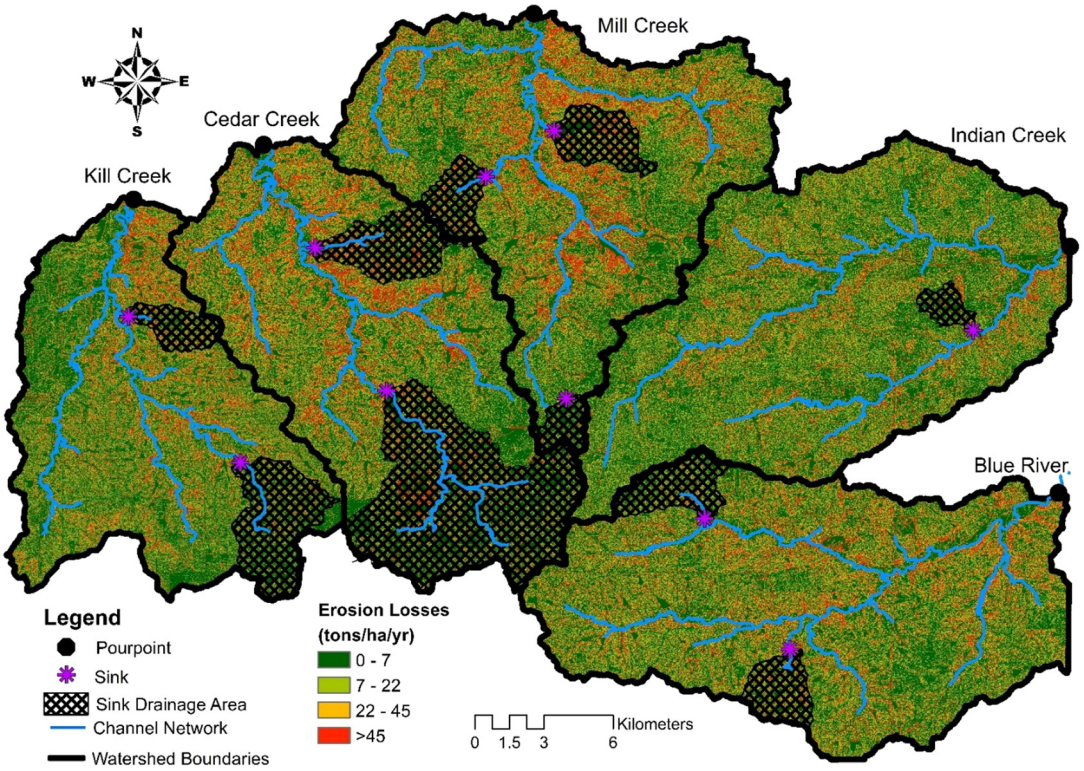

Fig. 4. Spatial distribution of mean erosion losses (tons/ha) as modeled by *RUSLE*. Sinks and their drainage areas are also plotted.

2017) that perform uncertainty analysis on *RUSLE* modeled erosion. To gain an understanding of the variable sediment erosion processes, for upland erosion at least, we conducted extensive Monte Carlo uncertainty analysis of *C* factor selection. The results showed that Mill Creek (std = 17.1 tons ha^{-1}) and Indian Creek (std = 14.8 tons ha^{-1}), the two most urban watersheds, had the highest variability in soil loss estimates. On the other hand, Kill Creek (std = 9.6 tons ha^{-1}) and Blue River (std = 11.9 tons ha^{-1}), the two most agriculturally dominated watersheds, had lowest uncertainties in the modeled erosion. This difference in variability is attributed mainly because there is much less agreement in *C* factor values for urban than for rural land uses in the *RUSLE* literature (Jain and Das, 2010; Soohoo et al., 2017). Further, since the *C* factor in *RUSLE* was originally formulated for agricultural cropland, the application of these factors to urban environments is generally more difficult and corresponds to larger uncertainties (Lisboa et al., 2017). In our literature review of 32 *RUSLE* studies, we found none that explicitly modeled the uncertainty of *C* factor variability. Most commonly, a single *C* factor that most closely resembled the investigated study site would be chosen from the literature and applied to the model watershed erosion (Alexakis et al., 2013; Biswas and Pani, 2015; Ozsahin et al., 2018). However, as *RUSLE* is an empirical equation in which each factor proportionally controls erosion estimates and we found several orders of magnitude difference within the same reported *C* factors from one study to the next. Thus, we highly recommend that

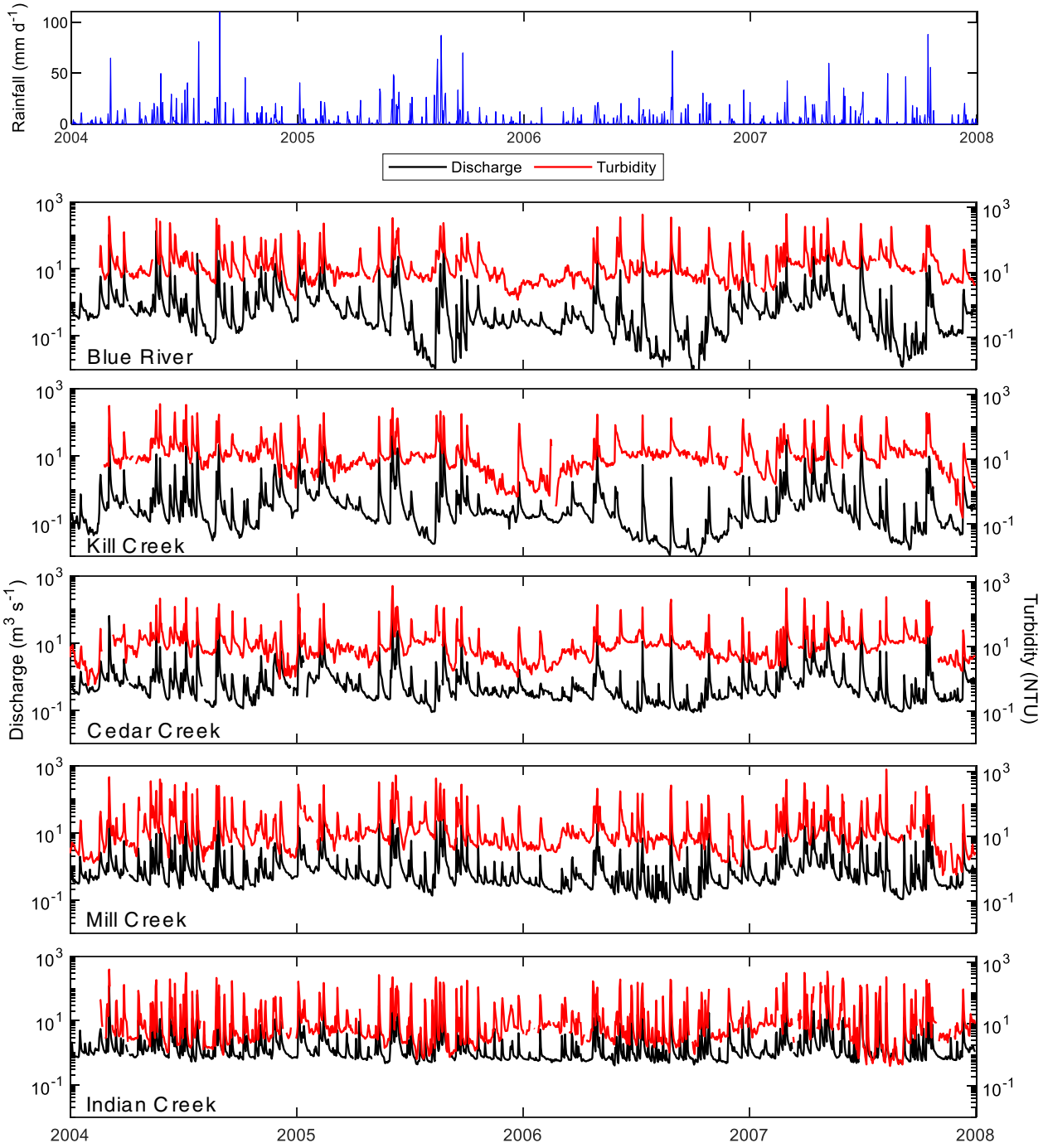

Fig. 5. Mean daily precipitation, stream discharge, and turbidity sensor data at the five watersheds from 2004 to 2008. Note: logarithmic y-axes are used to more readily distinguish patterns between sites.

watershed modelers and decision-makers consider performing Monte Carlo sampling to quantify uncertainties associated with *C* factor selection.

4.2. Sediment connectivity analysis

4.2.1. Sediment Delivery Ratio

Annual sediment yield, measured from continuous discharge and turbidity data, ranged from 7496 tons y^{-1} in Kill Creek up to 43,141 tons y^{-1} in Indian Creek (Table 2). The urban watersheds (Mill and Indian) tended to have higher baseflows, flashier events, and greater peak flows, which resulted in larger sediment concentrations than in the agricultural watersheds (Kill, Cedar, and Blue) (Fig. 5). This sediment yield combined with the prior analysis of erosion resulted in watershed-scale *SDR* values varying considerably from 0.03 to 0.15 (Table 2). Indian Creek, the most urbanized watershed, produced the highest *SDR* (0.15) whereas Kill Creek, the smallest and second-most rural watershed, produced the lowest *SDR* (0.03). The low overall *SDR*s indicate that at least 85 to 97% of sediment produced by upland rill and inter-rill erosion is subsequently deposited before reaching our monitoring stations. Actual storage is likely even greater as measured yield at the monitoring stations is a combination of upland and instream erosion, the latter of which is not considered in *RUSLE*. While this relative disconnectivity seems high, other studies in lowland settings have shown much greater storage with overall catchment delivery as low as 1% (Walling et al., 2006).

Regarding watershed-scale connectivity across land use, the *SDR* for urban watersheds (0.11) was typically double that of rural watersheds (0.06). Indian Creek is the most urbanized watershed and produced the highest measured yield and *SDR*, but also produced the lowest modeled erosion due to *RUSLE* not accounting for streambank erosion (Wischmeier and Smith, 1978). The high measured yield is likely because urbanization often leads to greater contribution of stream-bank erosion due to increased peak discharge and contribution of sediment-starved runoff from impervious surfaces (Mukundan et al., 2010). Though Mill Creek is also heavily urbanized, and likely contributes substantial streambank erosion, its *SDR* (0.07) is less than Indian Creek's and the same as the most-rural watershed, Blue River. The primary difference driving erosion between Mill Creek and Indian Creek is that *LS* factor for Mill Creek (1.34) is 50% greater than for Indian Creek (0.88), despite their equivalent average watershed gradients (3.5°; Table 1). This result indicates that much of the high-gradient Mill Creek slopes are near the primary channel and more well-connected to transport (Fig. 3c) as opposed to relatively disconnected erosion hot spots in Indian Creek. These results broadly agree with other work highlighting the importance of slope in impacting *SDR* with smaller values in lower-gradient watersheds (Hui et al., 2010). Thus, the spatiotemporal variability in the location and length of steep slopes can cause substantial erosion and connectivity differences even among watersheds with similar land use.

We used a watershed-scale *SDR* value to examine the impacts of land use and geomorphology on sediment dynamics and to serve as a proxy of sediment connectivity (Heckmann and Vericat, 2018; Wohl et al., 2019). Watershed-scale approximations of *SDR* integrate a multitude of factors that may have considerable in-watershed variation of vegetation, transport systems, material properties, and complex land surface interactions (Singh and Panda, 2017). Recently, more and more studies are highlighting the need to couple *RUSLE* predictions with *SDR* simulations to better represent and understand modeled erosion processes (Hamel et al., 2017; Zhao et al., 2020). Future work in estimating watershed-scale *SDR* should work to constrain uncertainty regarding how much of the measured yield is upland erosion versus stream bank erosion. Overall, our results indicate that as urbanization increases so does *SDR* and, by proxy, the maximum potential for sediment transport.

4.2.2. Index of Connectivity

Spatial structural connectivity patterns (from *IC* analysis) varied substantially depending on the choice of sink target: stream network (Fig. 6) or pour point (Fig. S2). With the higher order streams as targets,

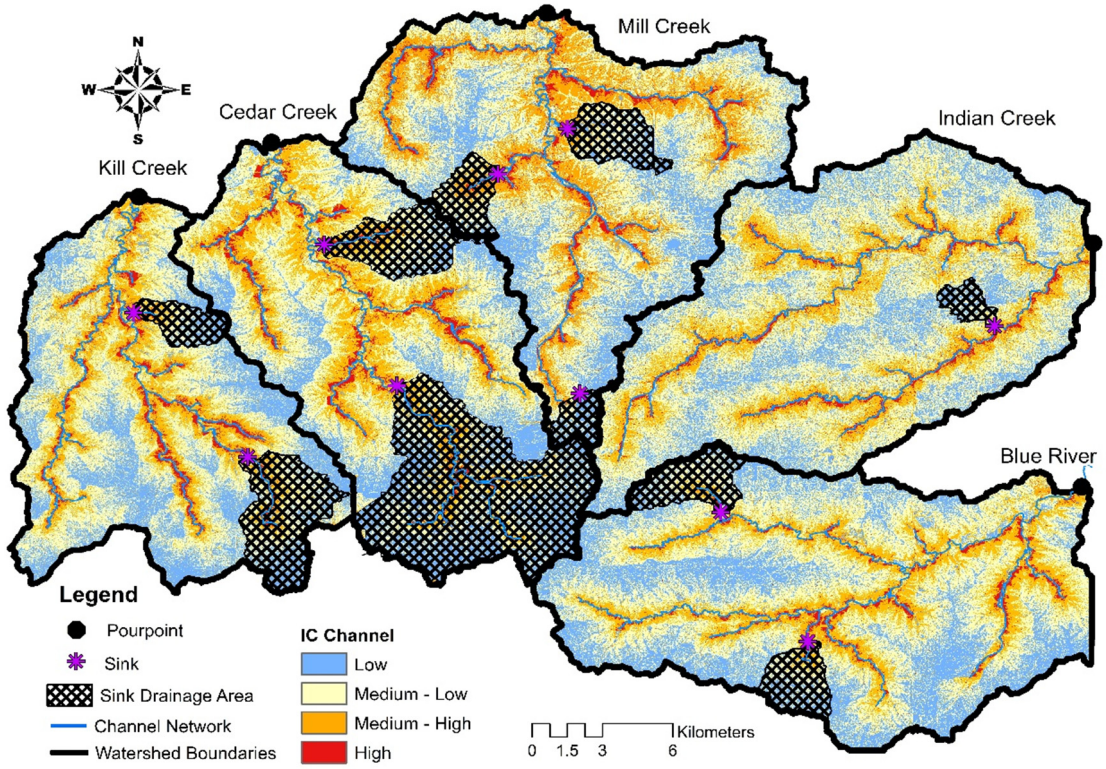

Fig. 6. Spatial distribution of Index of Connectivity (*IC*) for streamlines as targets. Sinks and their drainage areas are also plotted.

near-channel hillslopes were highly connected due to the proximity between particle origin and stream sink (Fig. 6). The average *IC* values using the stream channel network as targets were −5.92, −6.50, −5.83, −5.83, and −5.92 for Blue River, Kill Creek, Cedar Creek, Mill Creek, and Indian Creek, respectively. Conversely, analysis of the *IC* with watershed pourpoints resulted in the index being primarily driven by distance (Fig. S2), disconnecting much of the area and not allowing for analysis of local spatial patterns. For this reason, we proceed with our remaining analysis solely through the lens of stream-target connectivity as it more closely approximates hillslope coupling and (de)coupling processes (Cavalli et al., 2013). Further, spatial stream-target *IC* patterns have broad similarity with modeled erosion patterns (Fig. 4), highlighting the importance of slope gradients and lengths, which we recognize from our *SDR* analysis as influential to sediment transport. Lastly, we ran the *IC* tool twice, once with sinks (e.g. reservoirs, lakes shown in Fig. 1b) included in the analysis and another time with them excluded (results not shown). We found that there were no substantial differences in our lowland setting in overall structural connectivity with or without the sink drainage areas excluded.

IC modeling with stream targets paired with high resolution 1-m DEM data helped identify small scale rills and gullies as well as permanent man-made structures like roads and ditches (Fig. 6). Qualitative examination of the *IC* map demonstrates visual clarity of how roadways and urbanized surfaces are highlighted in the medium to high regime of connectivity as visible in northern Mill Creek and southern Cedar Creek. Further, the high-resolution *IC*-channel analysis was able to define flood plain areas as low connectivity. Furthermore, while pourpoint analysis is useful in mountainous areas with steep gradients (e.g. Cavalli et al., 2013; Tiranti et al., 2018), pourpoint analysis in our lowland watersheds (average slopes $< 5°$) results in high connectivity only near the target point. Unlike mountainous areas, which are driven primarily by natural processes, urbanizing areas can have anthropogenically augmented areas of connectivity distal to the watershed pourpoint and as such channel targets serve as a more accurate proxy for connectivity. The importance of selecting the correct sink target has shown to in other settings, such as in the case of road-drainage network intersections where roadways trap upslope material (Llena et al., 2019). In lowland agricultural settings as well as urban it may be necessary to specifically target channelized flow paths to gain an accurate representation especially at smaller spatial extents as seen in Calsamiglia et al. (2018).

It is important to note that *IC* is only a measure of structural connectivity, related to the arrangement of topographic features, and not a measure of functional connectivity, which would include the effects of dynamic processes that vary through space and time (Najafi et al., 2021). In this study, perturbations in system processes due to urbanization, such as increased capacity for runoff leading to small scale topographic changes, are unaccounted for due to the limitations in assessing only structural connectivity. Indian Creek, the most urbanized watershed, has relatively few areas extremely high *IC* due to the slope-driven nature of *IC* despite Indian Creek having the highest overall mean *IC* and sediment delivery (Fig. S3). Incorporation of process-based functional connectivity in this area could allow for the understanding of temporal and spatial evolution of urbanizing landscapes through examination of changes in storm event runoff and subsurface flow path (Husic et al., 2020). To extend the present work further and overcome the limitations of just analyzing structural connectivity, tools such as the probability of connectivity developed by Mahoney et al. (2018) could be incorporated into the analysis. The probability of connectivity concept combines structural and functional connectivity with the use of hydrologic models, such as SWAT, to assess the spatial and temporal variation in system components and processes dynamics (Mahoney et al., 2020a, 2020b). For our study, the primary objective was to obtain spatial representation of connectivity with easy to use and access tools rather than computationally demanding models. Thus, we did not perform functional connectivity analysis in this study although it an area of work that would further elucidate sediment processes in the studied watersheds.

A comparison between our watershed-scale connectivity proxy, *SDR*, and our main geospatial index, *IC*, were examined to understand trend patterns related to urbanization and sediment connectivity. *SDR* and *IC*, were positively related at the five sites ($R^2 = 0.78$, $p < 0.05$) with the highest *SDR* and *IC* in the most urbanized watershed (Fig. S3). *SDR* and *IC* have been linked in recent literature (Hamel et al., 2017; Zhao et al., 2020), but we find investigation in their linkages lacking, particularly in the context of urbanization and high-resolution modeling. Our linkage of a watershed-scale connectivity measure derived from in-stream monitoring data and *RUSLE* modeling (*SDR*) coupled to geomorphometric connectivity analysis (*IC*) provides a potential opportunity to estimate sediment conveyance in watersheds with only high-resolution DEM data availability (Meusburger et al., 2010; Cavalli et al., 2013). We partially attribute the *IC*-*SDR* relationship to landscape changes, which occur at a rapid time scale compared to natural geologic settings due to the removal of vegetation cover, the introduction of livestock and construction tracks, and development of housing and transport facilities. These changes create concentrated flow pathways which increase sediment transport capacity (Cavalli et al., 2013; van der Waal and Rowntree, 2018), resulting in larger values of *IC* (via continuous pathways to stream targets) and *SDR* (via reduced likelihood of temporary storage). This coupling appears to be stronger in more anthropogenically-impacted watersheds. We show a strong relationship between two independently derived connectivity indices and highlight how anthropogenic land use may control this relationship.

4.3. Sediment erosion and connectivity linkages

4.3.1. Erosion-Connectivity Mapping

The Erosion-Connectivity Biplots (ECBs) were an effective tool for visualizing the linkages and distributions of erosion and connectivity at the watershed-scale (Fig. 7). For normalized erosion, each watershed produced an exponential distribution bound by a value of zero. On the other hand, normalized *IC* distributions were right-skewed and, except for Cedar Creek, were slightly bimodal with a distinct smaller peak at higher *IC* values. Using the Jenks natural breaks algorithm to bifurcate the distributions, we were able to integrate the kernel distribution masses contained within each of the four identified quadrants: *E-C* = high erosion, high connectivity; *E-c* = high erosion, low connectivity; *e-C* = low erosion, high connectivity; and *e-c* = low erosion, low connectivity.

First, we investigated coupled erosion and connectivity, i.e., locations where the relative importance of both coincide and are either high (*E-C*) or low (*e-c*). For all watersheds, the bulk of land (59 to 68%) was in the *e-c* quadrant (Table 3), indicating that most of the study area is poorly erodible and poorly connected. Conversely, only 4 to 6% of watershed area was in the *E-C* quadrant, indicating that a small fraction of land is both highly erodible and highly connected. Thus, locations where erosion and connectivity are coupled constitute 64 to 72% of watershed area, but only a small fraction (4 to 6%) of that coupling contributes significantly to sediment transport. On the other hand, (de)coupled erosion and connectivity, i.e., locations where the relative importance of erosion and connectivity contradict (*e-C* or *E-c*), constituted the remaining 28 to 36% (Table 3). Of that remaining fraction, most (27 to 34%) was in the *e-C* quadrant with only a small amount (1.5 to 2.5%) in the *E-c* quadrant. In summary, areas with high erosion (*E-C* and *E-c*) make up 6 to 9% of the land area whereas locations with high connectivity (*E-C* and *e-C*) make up 31 to 39% of watershed area. These results indicate that more of the study area is well-connected than it is well-erodible, suggesting that erodibility of the landscape is a controlling factor of sediment transport in our study area.

Erosion-Connectivity Maps (ECMs) assisted in visualizing the spatial variability in erosion and connectivity linkages as determined by the ECBs (Fig. 8). Broadly, spatial ECM patterns are closely aligned with topography indicating that positive erosion-connectivity coupling is

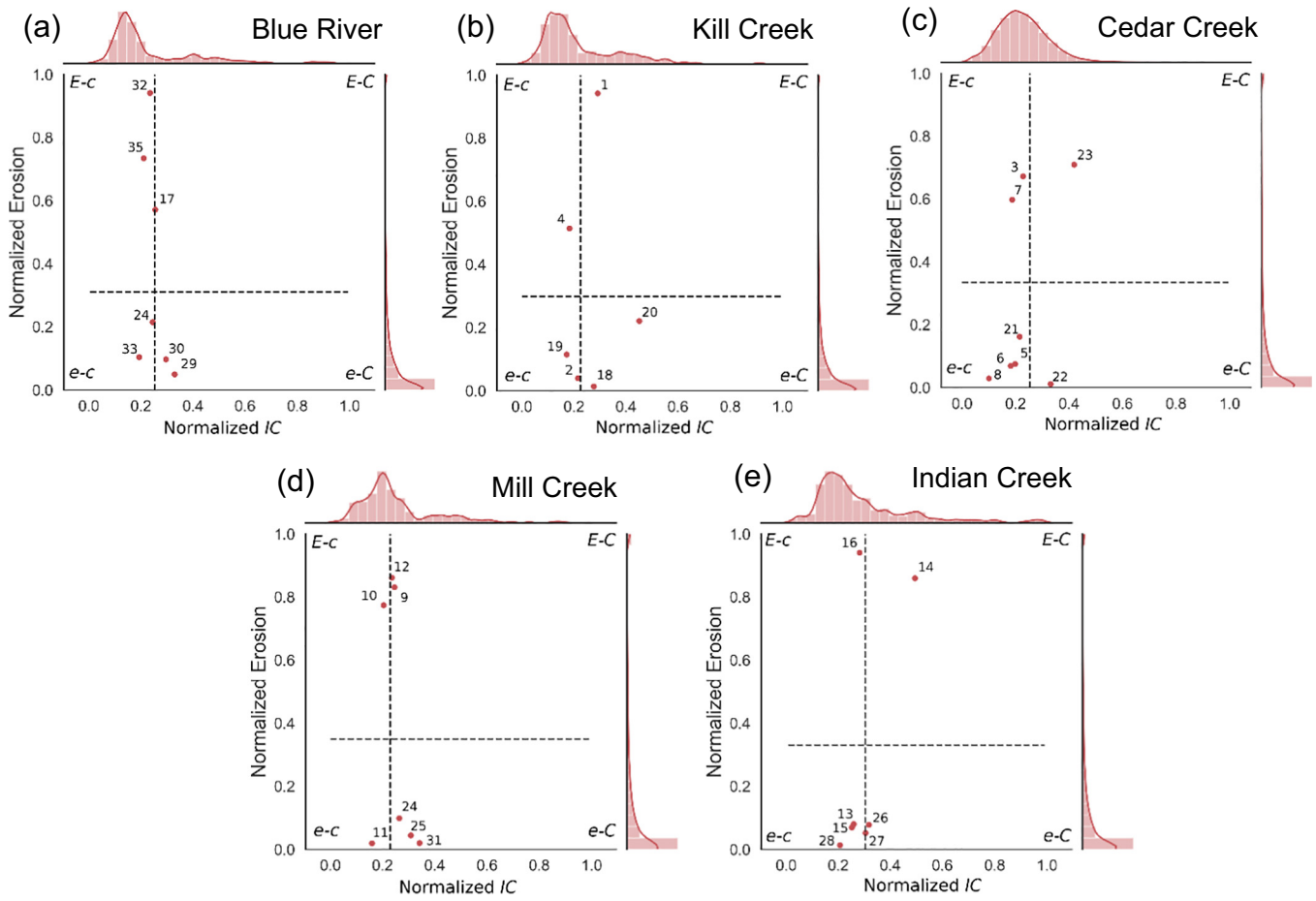

Fig. 7. Erosion-connectivity biplots (ECBs) across the five-watershed showing each field site ($n = 35$) as determined by the *RUSLE* and *IC* models. The marginal univariate plots indicate the distributions of all data points for erosion and connectivity per watershed: (a) Blue River, (b) Kill Creek, (c) Cedar Creek, (d) Mill Creek, and (e) Indian Creek. Dashed lines indicate the location of the Jenks natural breaks. Red dots indicated field site labelled with site number matching Fig. 8. Quadrant symbology: *E-C* = high erosion, high connectivity; *E-c* = high erosion, low connectivity; *e-C* = low erosion, high connectivity; and *e-c* = low erosion, low connectivity. (For interpretation of the references to colour in this figure legend, the reader is referred to the web version of this article.)

driven by landscape variability. Our ECM analysis suggests that most locations distal to higher order stream targets are both poorly connected and poorly erodible. However, not all near-stream areas are erodible, even if they are highly connected. Cedar Creek has the most potential for coupling of sediment erosion as it has the highest *E-C* proportion of all watersheds at 6.1% largely due to the high gradients and slope lengths near the primary stream corridors. On the other hand, Indian Creek has the second lowest *E-C* percentage potentially because of anthropogenic influences on the topography limit the length of fields for generating large amounts of surficial erosion as modeled by *RUSLE*. Indeed, the magnitude of the *LS* factor broadly agrees with the proportion of *E-C* land in a watershed due to the high likelihood of high slopes and lengths of fields coinciding with proximity to the primary stream corridor(s). Topographic features are indirectly related to land use through the altering of landscapes due to urbanization creating steeper sloping areas for urban area drainage. Further, roadways, ditches, and road-stream interactions in urbanized settings have been shown to be drivers of *IC* (Llena et al., 2019), which our results also show. To gain an improved understanding of how urbanization impacts the distribution of pathways, it would be helpful to have multiple LiDAR surveys over a period of many years to assess the change in connectivity networks over time as rills and ditches may form and develop new drainage networks (Lu et al., 2019; Zhao et al., 2020).

Our ECM analysis highlights that the coincident spatial location of topographic features that foster highly coupled erosion and connectivity are relatively rare (<6%; Fig. 8) but produce the most highly sensitive pathways, which disproportionately contribute sediment to downstream loading. For example, *E-C* quadrant areas are hot spots of erosion and our modeling indicates that 37±4% of all watershed erosion occurs in this 4 to 6% of watershed area. Recent physically-based hydrologic and sediment modeling also indicates the sensitivity of these relatively rare pathways to not only the magnitude of sediment delivery (Mahoney et al., 2020a), but also the timing of arrival (Mahoney et al., 2020b). Mahoney et al. (2018) found that even on the wettest day of the year, only 13% of the watershed area was connected to transport with that number dropping to 2% for the average rainfall event. Further, Mahoney et al. (2020b) found that these sensitive pathways are always important for transport irrespective of the rainfall depth, indicating that

Table 3
Analysis of the percent of each watershed's total area falling within an erosion-connectivity quadrant. Results are presented as the mean (±1σ) from twenty-five Monte Carlo realizations. Table symbology: *E-C* = high erosion, high connectivity; *E-c* = high erosion, low connectivity; *e-C* = low erosion, high connectivity; and *e-c* = low erosion, low connectivity.

Watershed	*E-C*	*E-c*	*e-C*	*e-c*
Blue River	5.2 ± 2.0	1.7 ± 2.0	34.1 ± 2.0	59.0 ± 2.0
Kill Creek	4.0 ± 1.4	2.0 ± 1.4	28.2 ± 1.3	65.7 ± 1.4
Cedar Creek	6.1 ± 1.6	1.9 ± 1.3	31.6 ± 1.6	60.3 ± 1.3
Mill Creek	6.0 ± 2.0	2.5 ± 1.7	31.3 ± 2.0	60.2 ± 1.7
Indian Creek	4.3 ± 1.4	1.5 ± 2.3	26.6 ± 1.5	67.7 ± 2.4

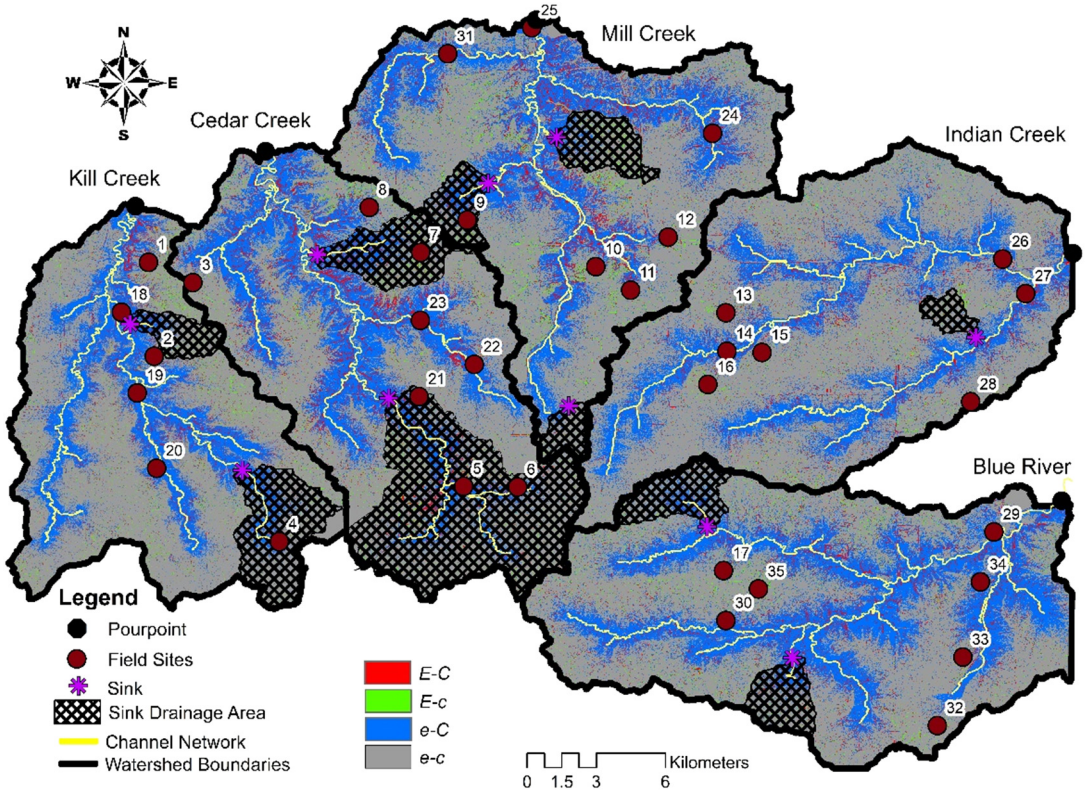

Fig. 8. Coupled erosion-connectivity map (ECM) showing the location of watershed pour points, field assessment sites (n = 35), streamlines used as targets for the index of connectivity analysis, delineated sink drainage areas, and quadrant analysis results. Legend symbology: *E-C* (red) = high erosion, high connectivity; *E-c* (green) = high erosion, low connectivity; *e-C* (blue) = low erosion, high connectivity; and *e-c* (grey) = low erosion, low connectivity. (For interpretation of the references to colour in this figure legend, the reader is referred to the web version of this article.)

identification of where these sensitive pathways occur is an important first step in managing them as they are not rainfall-dependent. Our ECM analysis provides a quick tool for this identification by integrating easy-to-implement analyses like the empirical *RUSLE* model and *SedInConnect IC* application. Other methods for this determination are temporally resolved but require physically-based numerical modeling, which must be calibrated with extensive data (e.g. Mahoney et al., 2020b). One reason that sensitive pathways are spatially constrained to fewer locations is because of the high likelihood of blockages (i.e. flow and sediment impedances, such as buffers, barriers, and blankets) to cause (dis)connectivity in the sediment cascade (Fryirs, 2012; Wohl et al., 2019). Because the *IC* metric is intrinsically linked to the flow pathway that a sediment particle would travel to the nearest sink, it integrates the possibility of these blockages to cause disconnection. However, as we will discuss in the next section, which includes our field assessment, the *IC* does not resolve these blockages entirely even with the use of high-resolution microtopography. This study provides a method for combining *RUSLE* and *IC* in a new ECM tool to identify coupling and (de)couplings of sediment production and transport to aid in management and understanding of watershed sedimentation.

4.3.2. Field assessment of erosion-connectivity

The average field assessment scores from our 35 sites, were 78 for erosion (ES) and 67 for connectivity (CS) (out of a maximum score of 150). While there were areas of agreement between the geospatial model and field assessments, field results indicate that current modeling tools (i.e. *RUSLE* and *IC*) need further refinement. Geospatial modeling results correctly predicted the field-observed intensity of erosion 51% of the time and connectivity 37% of the time. Connectivity performs worse as discontinuities to the sediment cascade (e.g. buffers, blankets, and barriers; Fryirs, 2012) are not explicitly incorporated into the *IC* formulation. This point is detailed more in the following paragraph where, for each of the four quadrants (*E-C*, *E-c*, *e-C*, *e-c*), we explore a site where the model accurately predicted field conditions and another site where it did not, and we explore discrepancies in predicted vs observed processes.

Fig. 9a shows an instance of strong agreement between model and field assessment for *E-C* (ES: 95, CS: 85) as steep slopes, visible rills and gullies, and exposed sediment sources at the site presented clear evidence of erosion processes and sediment transport with observed pathways overlapping with the model. Fig. 9b presents disagreement between the model and field assessment for *E-C* (ES: 70, CS: 55) where connectivity and erosion processes were not observed near the stream target due to flat slopes combined with dense vegetation buffers. Fig. S4a presents strong agreement between methods (ES: 95, CS: 50) for *E-c* with visible sediment erosion in the form of a gully combined with localized observed deposition. Disagreement between methods (ES: 95, CS: 90) for *E-c* (Fig. S4b) indicated under representation of connectivity for site 35 as transport pathways in the form of rills could be observed leading to subsurface drainage. Fig. S5a represents verification between model and field approaches (ES: 80, CS: 90) for *e-C* as visible pathways leading to an anthropogenic channel were observed, matching model output, while also observing lack of sediment sources in the area leading to less visible erosion. Disagreement between methods for *e-C* are seen in Fig. S5b (ES: 60, CS: 80) as the model over-represented connectivity near the stream target for site 18 with a dense vegetation buffer with no visible formation of pathways or sediment removal. Lastly, strong agreement between methods (ES: 70, CS: 45) for *e-c* areas was seen in a residential flood plain showing little erosion and heavy presence of deposition from surrounding areas (Fig. S6a). Fig. S6b represents disagreement between model and field approaches (ES: 90, CS: 85) for *e-c* by underestimating erosion and connectivity as visible construction equipment tracks showed the formation of rills

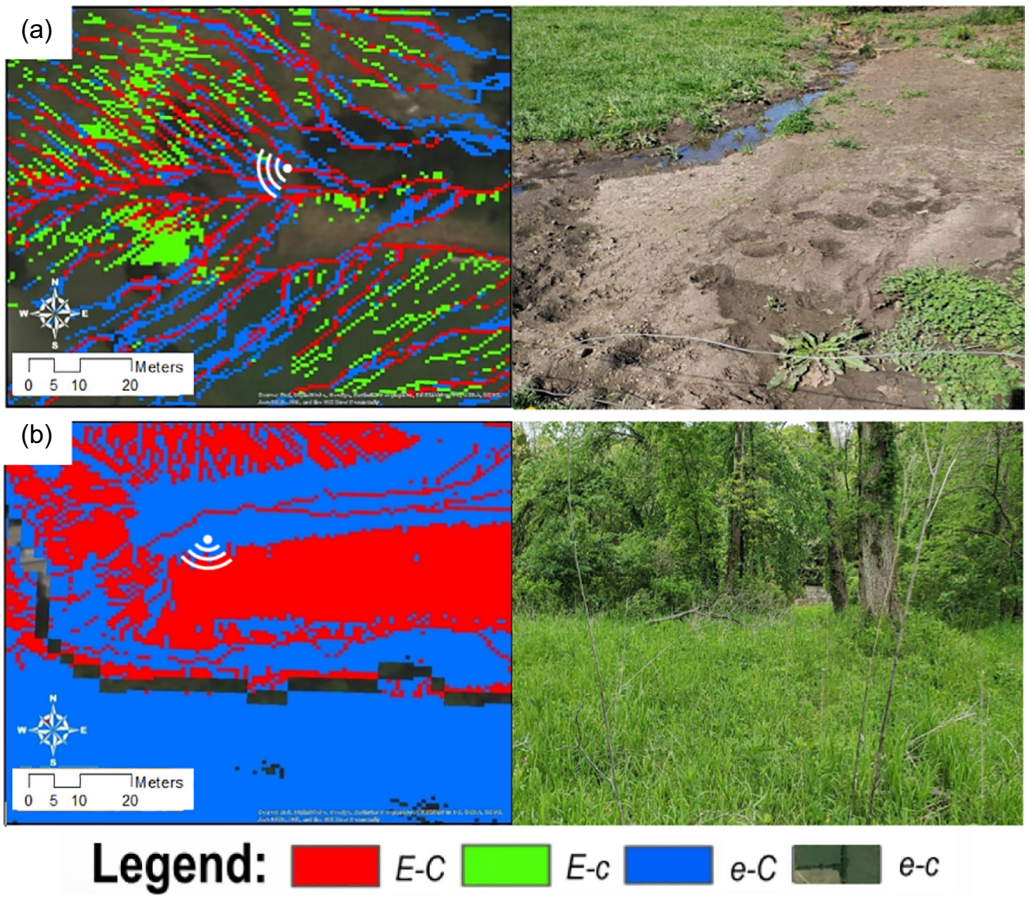

Fig. 9. Field assessment results for two *E-C* sites with modeled high erosion and high connectivity. (a) Site #3: a small gully in Cedar Creek. (b) Site #23: a heavily vegetated plain next to a channel in Cedar Creek. Each left panel represents geospatial model output with a white graphic that represents the field of view in the corresponding field assessment, located in the right panel.

with exposed sediment for erosion as well as connection to subsurface pathways.

The use of high-resolution data (i.e. 1-m in our model allowed for better reflection of microtopography and the landscape ability to accumulate water (Mahoney et al., 2018), thus we could observe exact erosion pathways in the field and the model leading to better agreement to real-world observations. Mahoney et al. (2018) further discusses this point by stating that low-resolution DEMs always overestimate connectivity and were supported by Cavalli et al. (2013) who found that high resolution data has the biggest impact on model accuracy. Additionally, high resolution impacts modeling related to urbanization as roadside channels can be resolved and thus increase erosion and connectivity simulated (Zhao et al., 2020). Lowland areas may be particularly sensitive to the effects of microtopography as high-sloping areas may be

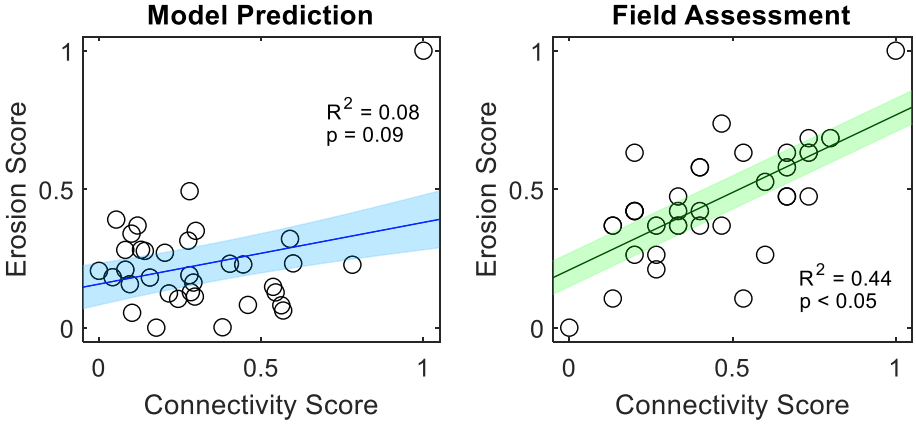

Fig. 10. Erosion and connectivity linkages as assessed by ECM model predictions and field validations at thirty-five sites. Modeled and field assessed scores are normalized between 0 and 1 for visual comparison. Each plot includes a linear regression with a 95% confidence interval. Model predictions indicated highly de-coupled erosion and connectivity dynamics for our sites. However, field assessments of the same locations show that erosion and connectivity were significantly coupled ($p < 0.05$), highlighting that present modeling tools underrepresent erosion and connectivity linkages.

relatively uncommon, but when they do occur, they tend to disproportionately contribute to sediment erosion and transport (Gay et al., 2016; Cossart et al., 2018), thus highlighting the need to represent them well.

Consequently, our field assessment also produced discrepancies when compared to model predictions and indicated that erosion and connectivity are more coupled in the field than models would suggest (Fig. 10). These discrepancies were largely due to the limitations in *RUSLE* and *IC* analysis, including how erosion-susceptibility, particularly land cover, and flow path blockages were represented in their respective models. Additionally, the discrepancies can be explained through the absence of hydrologic driven processes such as runoff due to precipitation as functional connectivity was not incorporated into this model. Recall that we purposefully selected our 35 field sites to span all four erosion-connectivity quadrants in the ECBs so that there would be no relation in modeled erosion and connectivity ($R^2 = 0.08$, $p = 0.09$; Fig. 10). If the model perfectly simulated field conditions, we would expect there to also be no relation during our field assessment; however, we find that our ECM map (constructed from *RUSLE* and *IC* results) underestimates the field-observed relation of erosion and connectivity ($R^2 = 0.44$, $p < 0.05$; Fig. 10). Regarding erosion prediction, the generalization of land cover causes issues regarding modeling as each land cover had multiple variations within it affecting modeled detachment accuracy (Soohoo et al., 2017). As NLCD data were relatively coarse (30-m), particularly compared to DEM resolution (1-m), improvements to modeling could include more on-the-ground assessment of land cover. Small features such as parks, agricultural fields, and construction sites have the potential for higher sediment erosion compared to larger aggregated surfaces and these small features may be masked under a coarse resolution, potentially underestimating erosion.

Regarding connectivity prediction, the *IC* model does not entirely resolve riparian or anthropogenic buffers, barriers, and blankets to the sediment cascade (Fryirs, 2012; Heckmann et al., 2018). These blockages cause (dis)connectivity and reduce the ability for sediment transport especially in areas located close to stream targets. The limitations of buffer presence can be resolved to some extent through the implementation of the relative smoothness index in the *IC* calculation, which accounts for impedance by utilizing Manning's n and has proven effective in forested watersheds (Zanandrea et al., 2020). Further limitations related to the topographic modeling is that urban area subsurface pathways, such as stormwater drainage, are unaccounted *IC* targets which create transverse pathways that likely increase *IC* values, but are not captured from DEM data alone (Calsamiglia et al., 2018). This latter argument can be remedied as flexibility in the *SedInConnect* tool allows for any type of target to be added, including subsurface flow pathways if their accurate mapping exists. Another limitation related to unexpected observations is the temporal aspect of urbanization. In urbanizing areas, construction is an ongoing process which creates exposed tracks in sediment that concentrate runoff and aid in the development of rills and gullies producing increased erosion and sediment pathways (Marchamalo et al., 2016) that are not represented after the date when LiDAR data is recorded. To better analyze structural connectivity, the use of temporal variations needs to be incorporated with the spatial variability (Mahoney et al., 2020a, 2020b). Furthermore, *IC* was not a good estimate for inter-rill areas as they are more difficult to detect as the microtopography can be altered in a short time span under high sediment fluxes (Lu et al., 2019). While the ECM tool could be improved by the inclusion of subsurface flow paths and better discretization of microtopographic features, it nonetheless provides useful estimates of the spatial linkages of erosion and connectivity.

5. Conclusions

Overall, this study aimed to understand how sediment erosion and connectivity were linked across an urbanizing lowland landscape and led to the following conclusions:

1) *RUSLE* modeling results show that for lowland urbanizing watersheds topography is the primary driver of erosion with the largest uncertainties associated with urban *C* factor representation. We recommend assessing uncertainty in *RUSLE* predictions with Monte Carlo sampling of *C* factors as urban influence is not well-defined in the *RUSLE* literature. Additionally, *RUSLE* has limitations when applied to larger watersheds related to the scaling of processes, which could be improved by utilizing more physically-based erosion models operating at finer timescales.
2) *IC* results indicate that for lowland areas streamlines are more appropriate sink targets than watershed pourpoints as they more accurately represent sediment pathways. The studied connectivity metrics, *IC* and *SDR*, were positively related and generally indicated that the most anthropogenically-impacted watersheds were also more efficient at conveying sediment from source to sink. However, we assessed only static/topographic connectivity and more work is needed to see if urban watersheds remain more effective conveyors during dynamic conditions as assessed by functional connectivity.
3) We developed an Erosion-Connectivity Mapping framework that provides a new method for spatially quantifying coupling and (de) coupling of sediment erosion and connectivity using publicly available datasets. Modeling results indicate that erosion is more likely to be the limiting factor in sediment transport, as opposed to connectivity, as there are generally more locations that are well-connected to hydrologic transport but resistant to erosion. However, since *RUSLE* does not account for channelized erosion and *IC* only considers structural connectivity, additional investigation is needed to understand this relationship. The ECMs performed with relative accuracy as validated by field assessment and bridge the gap in the literature between the *RUSLE* and *IC* methodologies.
4) Field assessment of the ECMs indicated that geospatial modeling underpredicts how closely related erosion and connectivity are in the field because geospatial models do not resolve all buffers, barriers, and blankets in the sediment cascade. We suggest that future improvements be made to *RUSLE* and *IC* models to consider this greater coupling more explicitly.

CRediT authorship contribution statement

A. Michalek: Conceptualization, Methodology, Data curation, Writing – original draft, Writing – review & editing, Visualization. **A. Zarnaghsh:** Conceptualization, Methodology, Data curation. **A. Husic:** Conceptualization, Methodology, Data curation, Writing – original draft, Writing – review & editing, Visualization, Supervision, Project administration.

Declaration of competing interest

The authors declare that they have no known competing financial interests or personal relationships that could have appeared to influence the work reported in this paper.

Acknowledgments

We would like to thank Associate Editor Paulo Pereira and two anonymous reviewers for their constructive comments that helped improve the quality of this manuscript. Further, we thank the University of Kansas Department of Civil, Environmental, and Architectural Engineering for providing partial funding to the student authors of the manuscript. We also gratefully acknowledge Teresa Rasmussen of the USGS Kansas Water Science Center for assisting with the aquatic sensor data used in this project. Additionally, we would like to acknowledge Johnson County AIMS and the Stormwater Management Program for providing us with the high-resolution LiDAR data used in this study. Lastly, we thank Erin Reinkemeyer, Brian Fairchild, and Oladipo Bolade for helping

to aggregate land management factors used in the *RUSLE* modeling. We declare no competing financial or personal conflicts of interests.

Appendix A. Supplementary data

Supplementary data to this article can be found online at https://doi.org/10.1016/j.scitotenv.2020.144255.

References

AIMS, 2020. Johnson County Automated Information Mapping System. https://maps.jocogov.org/ims/.

Alexakis, D.D., Hadjimitsis, D.G., Agapiou, A., 2013. Integrated use of remote sensing, GIS and precipitation data for the assessment of soil erosion rate in the catchment area of "Yialias" in Cyprus. Atmos. Res. 131, 108–124. https://doi.org/10.1016/j.atmosres.2013.02.013.

Alk, M.G.F., Enham, R.J.D., Engersen, K.L.M., 2009. Estimating uncertainty in the revised universal soil loss equation via Bayesian melding. J. Agric. Biol. Environ. Stat. 15, 20–37. https://doi.org/10.1007/s13253-009-0005-y.

Baartman, J.E.M., Masselink, R., Keesstra, S.D., Temme, A.J.A.M., 2013. Linking landscape morphological complexity and sediment connectivity. Earth Surf Process Landforms 38, 1457–1471. https://doi.org/10.1002/esp.3434.

Beskow, S., Mello, C.R., Norton, L.D., Curi, N., Viola, M.R., Avanzi, J.C., 2009. Soil erosion prediction in the Grande River Basin, Brazil using distributed modeling. Catena 79, 49–59. https://doi.org/10.1016/j.catena.2009.05.010.

Biswas, S.S., Pani, P., 2015. Estimation of soil erosion using RUSLE and GIS techniques: a case study of Barakar River basin, Jharkhand, India. Model Earth Syst Environ 1, 1–13. https://doi.org/10.1007/s40808-015-0040-3.

Bordoni, M., Giuseppina Persichillo, M., Meisina, C., Crema, S., Cavalli, M., Bartelletti, C., Galanti, Y., Barsanti, M., Giannecchini, R., D'Amato Avanzi, G., 2018. Estimation of the susceptibility of a road network to shallow landslides with the integration of the sediment connectivity. Nat. Hazards Earth Syst. Sci. 18, 1735–1758. https://doi.org/10.5194/nhess-18-1735-2018.

Borrelli P, Robinson DA, Fleischer LR, Lugato E, Ballabio C, Alewell C, Meusburger K, Modugno S, Schütt B, Ferro V, Bagarello V, Oost K Van, Montanarella L, Panagos P (2012) Land use change on soil erosion. Nat. Commun.. doi: https://doi.org/10.1038/s41467-017-02142-7.

Borselli, L., Cassi, P., Torri, D., 2008. Prolegomena to sediment and flow connectivity in the landscape: A GIS and field numerical assessment. Catena 75, 268–277. https://doi.org/10.1016/j.catena.2008.07.006.

Brierley, G., Fryirs, K., Jain, V., 2006. Landscape connectivity: the geographic basis of geomorphic applications. Area 38, 165–174. https://doi.org/10.1111/j.1475-4762.2006.00671.x.

Calsamiglia, A., García-Comendador, J., Fortesa, J., López-Tarazón, J.A., Crema, S., Cavalli, M., Calvo-Cases, A., Estrany, J., 2018. Effects of agricultural drainage systems on sediment connectivity in a small Mediterranean lowland catchment. Geomorphology 318, 162–171. https://doi.org/10.1016/j.geomorph.2018.06.011.

Cavalli, M., Trevisani, S., Comiti, F., Marchi, L., 2013. Geomorphometric assessment of spatial sediment connectivity in small Alpine catchments. Geomorphology 188, 31–41. https://doi.org/10.1016/j.geomorph.2012.05.007.

Cossart, E., Viel, V., Lissak, C., Reulier, R., Fressard, M., Delahaye, D., 2018. How might sediment connectivity change in space and time? L Degrad Dev 29, 2595–2613. https://doi.org/10.1002/ldr.3022.

Crema, S., Cavalli, M., 2018. SedInConnect: a stand-alone, free and open source tool for the assessment of sediment connectivity. Comput. Geosci. 111, 39–45. https://doi.org/10.1016/j.cageo.2017.10.009.

Di Stefano, C., Ferro, V., 2019. Assessing sediment connectivity in dendritic and parallel calanchi systems. Catena 172, 647–654. https://doi.org/10.1016/j.catena.2018.09.023.

ESRI, 2006. ArcGIS Mapping Software. https://www.esri.com/en-us/arcgis/about-arcgis/overview.

Fryirs, K., 2012. (Dis)connectivity in catchment sediment cascades: a fresh look at the sediment delivery problem. Earth Surf Process Landforms 38, 30–46. https://doi.org/10.1002/esp.3242.

Gay, A., Cerdan, O., Mardhel, V., Desmet, M., 2016. Application of an index of sediment connectivity in a lowland area. J. Soils Sediments 16, 280–293. https://doi.org/10.1007/s11368-015-1235-y.

Grauso, S., Pasanisi, F., Tebano, C., 2018. Assessment of a simplified connectivity index and specific sediment potential in river basins by means of geomorphometric tools. Geosci 8. https://doi.org/10.3390/geosciences8020048.

Hamel, P., Falinski, K., Sharp, R., Auerbach, D.A., Sánchez-canales, M., Dennedy-frank, P.J., 2017. Science of the total environment sediment delivery modeling in practice : comparing the effects of watershed characteristics and data resolution across hydroclimatic regions. Sci. Total Environ. 580, 1381–1388. https://doi.org/10.1016/j.scitotenv.2016.12.103.

Harrison, R.L., 2009. Introduction to Monte Carlo simulation. AIP Conf Proc 1204, 17–21. https://doi.org/10.1063/1.3295638.

Heathcote, A.J., Filstrup, C.T., Downing, J.A., 2013. Watershed Sediment Losses to Lakes Accelerating despite Agricultural Soil Conservation Efforts. vol. 8, pp. 1–4. https://doi.org/10.1371/journal.pone.0053554.

Heckmann, T., Vericat, D., 2018. Computing spatially distributed sediment delivery ratios: inferring functional sediment connectivity from repeat high-resolution digital elevation models. Earth Surf Process Landforms 43, 1547–1554. https://doi.org/10.1002/esp.4334.

Heckmann, T., Cavalli, M., Cerdan, O., Foerster, S., Javaux, M., Lode, E., Smetanová, A., Vericat, D., Brardinoni, F., 2018. Indices of sediment connectivity: opportunities, challenges and limitations. Earth-Science Rev 187, 77–108. https://doi.org/10.1016/j.earscirev.2018.08.004.

Hu, S., Zhi-mao, G., Jun-ping, Y., 2001. The impacts of urbanization on soil erosion in the Loess Plateau region. J. Geogr. Sci. 11, 282–290. https://doi.org/10.1007/bf02892311.

Hui, L., Xiaoling, C., Lim, K.J., Xiaobin, C., Sagong, M., 2010. Assessment of soil erosion and sediment yield in Liao watershed, Jiangxi Province, China, using USLE, GIS, and RS. J. Earth Sci. 21, 941–953. https://doi.org/10.1007/s12583-010-0147-4.

Husic, A., Fox, J., Mahoney, T., Gerlitz, M., Pollock, E., Backus, J., 2020. Optimal transport for assessing nitrate source-pathway connectivity. Water Resour. Res. 56 (10), e2020WR027446. https://doi.org/10.1029/2020WR027446.

Jain, M.K., Das, D., 2010. Estimation of sediment yield and areas of soil erosion and deposition for watershed prioritization using GIS and remote sensing. Water Resour. Manag. 24, 2091–2112. https://doi.org/10.1007/s11269-009-9540-0.

Jenks, G.F., 1967. The data model concept in statistical mapping. International Yearbook of Cartography 7, 186–190.

Jiang, L., O'Neill, B.C., 2017. Global urbanization projections for the Shared Socioeconomic Pathways. Glob. Environ. Chang. 42, 193–199. https://doi.org/10.1016/j.gloenvcha.2015.03.008.

Lisboa, E.G., Blanco, C.J.C., Maia, R.O.P., Bello, L.A.L., 2017. A stochastic estimation of sediment production in an urban catchment using the USLE model. Hydrol. Sci. J. 62, 2571–2586. https://doi.org/10.1080/02626667.2017.1395031.

Llena, M., Vericat, D., Cavalli, M., Crema, S., Smith, M.W., 2019. The effects of land use and topographic changes on sediment connectivity in mountain catchments. Sci. Total Environ. 660, 899–912. https://doi.org/10.1016/j.scitotenv.2018.12.479.

López-Vicente, M., Poesen, J., Navas, A., Gaspar, L., 2013. Predicting runoff and sediment connectivity and soil erosion by water for different land use scenarios in the Spanish Pre-Pyrenees. Catena 102, 62–73. https://doi.org/10.1016/j.catena.2011.01.001.

Lu, X., Li, Y., Washington-Allen, R.A., Li, Y., 2019. Structural and sedimentological connectivity on a rilled hillslope. Sci. Total Environ. 655, 1479–1494. https://doi.org/10.1016/j.scitotenv.2018.11.137.

Mahoney, D.T., 2020. Probabilistic Approach to Water, Sediment, and Nutrient Connectivity for Advancing Watershed Modelling. PhD Dissertation. University of Kentucky, Lexington, Kentucky.

Mahoney, D.T., Fox, J.F., Al Aamery, N., 2018. Watershed erosion modeling using the probability of sediment connectivity in a gently rolling system. J. Hydrol. 561, 862–883. https://doi.org/10.1016/j.jhydrol.2018.04.034.

Mahoney, T., Fox, J., Al-Aamery, N., Clare, E., 2020a. Integrating connectivity theory within watershed modelling part I: model formulation and investigating the timing of sediment connectivity. Sci. Total Environ., 140385 https://doi.org/10.1016/j.scitotenv.2020.140385.

Mahoney, T., Fox, J., Al-Aamery, N., Clare, E., 2020b. Integrating connectivity theory within watershed modelling part II: application and evaluating structural and functional connectivity. Sci. Total Environ., 140386 https://doi.org/10.1016/j.scitotenv.2020.140386.

Marchamalo, M., Hooke, J.M., Sandercock, P.J., 2016. Flow and sediment connectivity in semi-arid landscapes in SE Spain: patterns and controls. L Degrad Dev 27, 1032–1044. https://doi.org/10.1002/ldr.2352.

Martin, C., Ayesa, E., 2010. An integrated Monte Carlo methodology for the calibration of water quality models. Ecol. Model. 221, 2656–2667. https://doi.org/10.1016/j.ecolmodel.2010.08.008.

Messenzehl, K., Hoffmann, T., Dikau, R., 2014. Sediment connectivity in the high-alpine valley of Val Müschauns, Swiss National Park - linking geomorphic field mapping with geomorphometric modelling. Geomorphology 221, 215–229. https://doi.org/10.1016/j.geomorph.2014.05.033.

Meusburger, K., Konz, N., Schaub, M., Alewell, C., 2010. Soil erosion modelled with USLE and PESERA using QuickBird derived vegetation parameters in an alpine catchment. Int. J. Appl. Earth Obs. Geoinf. 12, 208–215. https://doi.org/10.1016/j.jag.2010.02.004.

Mishra, K., Sinha, R., Jain, V., Nepal, S., Uddin, K., 2019. Towards the assessment of sediment connectivity in a large Himalayan river basin. Sci. Total Environ. 661, 251–265. https://doi.org/10.1016/j.scitotenv.2019.01.118.

Mukundan, R., Radcliffe, D.E., Ritchie, J.C., Risse, L.M., McKinley, R.A., 2010. Sediment fingerprinting to determine the source of suspended sediment in a southern Piedmont stream. J. Environ. Qual. 39, 1328–1337. https://doi.org/10.2134/jeq2009.0405.

Najafi, S., Dragovich, D., Heckmann, T., Sadeghi, S.H., 2021. Sediment connectivity concepts and approaches. Catena 196, 104880. https://doi.org/10.1016/j.catena.2020.104880.

Napoli, M., Cecchi, S., Orlandini, S., Mugnai, G., Zanchi, C.A., 2016. Catena simulation of field-measured soil loss in Mediterranean hilly areas (Chianti, Italy) with RUSLE. Catena 145, 246–256. https://doi.org/10.1016/j.catena.2016.06.018.

NLCD, 2015. Multi-Resolution Land Characteristics (MRLC) Consortium. https://www.mrlc.gov/.

Ozcan, A.U., Erpul, G., Basaran, M., Erdogan, H.E., 2008. Use of USLE/GIS technology integrated with geostatistics to assess soil erosion risk in different land uses of Indagi Mountain Pass - Çankiri, Turkey. Environ. Geol. 53, 1731–1741. https://doi.org/10.1007/s00254-007-0779-6.

Ozsahin, E., Duru, U., Eroglu, I., 2018. Land use and land cover changes (LULCC), a key to understand soil erosion intensities in the Maritsa Basin. Water https://doi.org/10.3390/w10030335.

Papadopoulos, C.E., Yeung, H., 2001. Uncertainty estimation and Monte Carlo simulation method. Flow Meas. Instrum. 12, 291–298. https://doi.org/10.1016/S0955-5986(01)00015-2.

Rasmussen, T., Gatotho, J., 2014. Water-quality variability and constituent transport and processes in streams of Johnson County, Kansas, using continuous monitoring and regression models, 2003-11. US Geol. Surv. Sci. Investig. Rep., 2013–5221 https://doi.org/10.3133/sir20135221.

Renard, K.G., Foster, G.R., Weesies, G.A., Mccool, D.K., Yoder, D.C., 1997. Predicting Soil Erosion by Water: A Guide to Conservation Planning with the Revised Universal Soil Loss Equation (RUSLE). Agricultural Handbook 703. US Department of Agriculture.

Renard KG, Foster GR, Weesies GA, Porter JI (2008) Revised universal soil loss equation (Rusle). Encycl Earth Sci Ser 607–608. doi: https://doi.org/10.1007/springerreference_77104.

Rizeei, H.M., Saharkhiz, M.A., Pradhan, B., Ahmad, N., 2016. Soil erosion prediction based on land cover dynamics at the Semenyih watershed in Malaysia using LTM and USLE models. Geocarto Int 31, 1158–1177. https://doi.org/10.1080/10106049.2015.1120354.

Rommens, T., Verstraeten, G., Bogman, P., Peeters, I., Poesen, J., Govers, G., Van Rompaey, A., Lang, A., 2006. Holocene alluvial sediment storage in a small river catchment in the loess area of Central Belgium. Geomorphology 77, 187–201. https://doi.org/10.1016/j.geomorph.2006.01.028.

Singh, G., Panda, R.K., 2017. Grid-cell based assessment of soil erosion potential for identification of critical erosion prone areas using USLE, GIS and remote sensing: a case study in the Kapgari watershed, India. Int Soil Water Conserv Res 5, 202–211. https://doi.org/10.1016/j.iswcr.2017.05.006.

Smith, D., Wischmeier, W.H., 1962. Rainfall Erosion. Advances in Agronomy, pp. 109–148.

Soohoo, W.M., Wang, C., Li, H., 2017. Geospatial assessment of bioenergy land use and its impacts on soil erosion in the U. S. Midwest. J. Environ. Manag. 190, 188–196. https://doi.org/10.1016/j.jenvman.2016.12.057.

StormWatch, 2020. Johnson County, Kansas StormWATCH. https://www.stormwatch.com/home.php.

Tarolli, P., Cavalli, M., Masin, R., 2019. High-resolution morphologic characterization of conservation agriculture. Catena 172, 846–856. https://doi.org/10.1016/j.catena.2018.08.026.

Tiranti, D., Crema, S., Cavalli, M., Deangeli, C., 2018. An integrated study to evaluate debris flow hazard in alpine environment. Front. Earth Sci. 6, 1–14. https://doi.org/10.3389/feart.2018.00060.

USDA, 2018. USDA web soil survey. https://www.nrcs.usda.gov/wps/portal/nrcs/main/soils/survey/. (Accessed 20 September 2018).

USGS, 2018. National Water Information System data available on the World Wide Web (USGS Water Data for the Nation). https://waterdata.usgs.gov/nwis/. (Accessed 20 September 2018).

van der Waal, B., Rowntree, K., 2018. Landscape connectivity in the Upper Mzimvubu River Catchment: an assessment of anthropogenic influences on sediment connectivity. L Degrad Dev 29, 713–723. https://doi.org/10.1002/ldr.2766.

Walling, D.E., Collins, A.L., Jones, P.A., Leeks, G.J.L., Old, G., 2006. Establishing fine-grained sediment budgets for the Pang and Lambourn LOCAR catchments, UK. J. Hydrol. 330, 126–141. https://doi.org/10.1016/j.jhydrol.2006.04.015.

Wischmeier, W.H., Smith, D., 1978. Predicting Rainfall Erosion Losses—A Guide to Conservation Planning. No. 537. Department of Agriculture, Science and Education Administration.

Wohl, E., Brierley, G., Cadol, D., Coulthard, T.J., Covino, T., Fryirs, K.A., Grant, G., Hilton, R.G., Lane, S.N., Magilligan, F.J., Meitzen, K.M., Passalacqua, P., Poeppl, R.E., Rathburn, S.L., Sklar, L.S., 2019. Connectivity as an emergent property of geomorphic systems. Earth Surf Process Landforms 44, 4–26. https://doi.org/10.1002/esp.4434.

Yuan, L., Yang, G., Zhang, Q., Li, H., 2016. Soil erosion assessment of the Poyang Lake Basin, China: using USLE, GIS and remote sensing. J Remote Sens GIS 5. https://doi.org/10.4172/2469-4134.1000168.

Zanandrea, F., Michel, G.P., Kobiyama, M., 2020. Impedance influence on the index of sediment connectivity in a forested mountainous catchment. Geomorphology 351, 106962. https://doi.org/10.1016/j.geomorph.2019.106962.

Zeng, C., Wang, S., Bai, X., Li, Y., Tian, Y., Li, Y., Wu, L., 2017. Soil erosion evolution and spatial correlation analysis in a typical karst geomorphology using RUSLE with GIS. Solid Earth 8, 721–736.

Zerihun, M., Mohammedyasin, M.S., Sewnet, D., Adem, A.A., 2018. Geoderma regional assessment of soil erosion using RUSLE , GIS and remote sensing in NW Ethiopia. Geoderma Reg 12, 83–90. https://doi.org/10.1016/j.geodrs.2018.01.002.

Zhao, G., Gao, P., Tian, P., Sun, W., Hu, J., Mu, X., 2020. Assessing sediment connectivity and soil erosion by water in a representative catchment on the Loess Plateau, China. Catena 185. https://doi.org/10.1016/j.catena.2019.104284.